Experimental Thermal and Fluid Science 103 (2019) 163–181

Contents lists available at ScienceDirect

Experimental Thermal and Fluid Science

journal homepage: www.elsevier.com/locate/etfs

# On the flow physics and vortex behavior of rectangular orifice synthetic jets

Abhay Kumar[a], Arun K. Saha[b], Pradipta Kumar Panigrahi[b], Ashish Karn[a,*]

[a] Department of Mechanical Engineering, University of Petroleum and Energy Studies, Energy Acres, Bidholi, Dehradun, Uttarakhand 248007, India
[b] Department of Mechanical Engineering, Indian Institute of Technology Kanpur, Uttar Pradesh 248007, India

ARTICLE INFO

*Keywords:*
Synthetic jet
Vortex rings
Rectangular orifice
Bifurcation
Vortex

ABSTRACT

Synthetic jet actuators possess a continuous jet like behavior in its far region and have found wide-scale engineering applications since it allows momentum transport to the flow system without any net mass transfer across the flow boundaries. The case of a non-axisymmetric synthetic jet is particularly significant since it is affected by the differential shear layer at the orifice exit, that depends on its aspect ratio. However, despite exhaustive research on both continuous and synthetic jets, very few studies have experimentally investigated the case of rectangular orifice synthetic jets, focusing on the effect of aspect ratio of the orifice as well as the actuation frequency upon the vortex behavior and the flow physics. In particular, the intriguing phenomenon of vortex bifurcation has mostly been reported only for an individual vortex or for a plain jet. Yet, in a train of vortex rings, such as that obtained in a synthetic jet, the occurrence of vortex bifurcation can be expected, although the flow physics in the wake of individual vortex rings is significantly different. The present study experimentally investigates a rectangular orifice synthetic jet at different orifice aspect ratios and actuation frequencies, focusing on exploring the conditions at which vortex bifurcation occurs, through LIF imaging and Hot-film measurements. The primary objective of these experiments is to provide a qualitative physical insight into the synthetic jet ejected from a rectangular orifice (through LIF imaging), as well as to quantitatively explore the experimental conditions that promote different flow structures (through velocity time trace, time-averaged velocity profiles and power spectral density measurements), particularly the bifurcation of vortex rings. Our experiments indicate that the phenomenon of vortex bifurcation is observed during the axial switching of vortex rings, but only in a narrow range of experimental conditions. Further, the velocity measurements have ascertained that the two prominent reasons behind this bifurcation process are a large disparity in the velocities of the vortex core and the center of vortex ring, as well as the time lag in which the separation distance between the counter-rotating vortices decrease gradually to zero.

## 1. Introduction

A synthetic jet can be defined as a train of vortex rings that originates completely from the working fluid, carries no net mass flux and yet transfers linear momentum to the fluid flow. A synthetic jet actuation system that typically consists of a mechanism to change the volume of chamber either through a piston or through a flexible diaphragm. As the oscillating boundary of the cavity moves away from the orifice, thus increasing the volume, fluid from the surrounding is sucked into the cavity. The fluid is subsequently ejected out when the oscillating boundary moves towards the orifice reducing the volume of the chamber. During the ejection period, the shear layer formed around the orifice circumference due to finite thickness of the orifice plate separates at the sharp edges of the orifice and rolls up into vortex rings. These vortex rings move away from the orifice under their self-induced velocity thus synthesizing a jet of fluid through the entrainment of the ambient fluid. It is also called a Zero Net Mass Flux (ZNMF) jet, since it is formed entirely from the ambient working fluid of the flow system allowing momentum transport to the flow system without any net mass transfer across the flow boundaries. Consequently, in contrast to other jet flows, it is a preferred choice in many engineering applications such as flow separation control over bluff bodies [2], stalled airfoils [3], duct flow [1,11], maneuverability of Unmanned Aerial Vehicles [9,17], jet-vectoring [20], mixing enhancement [8] and in electronic cooling [4].

In the existing literature, a plethora of work on synthetic jets has already been reported. Many of these studies underline the importance of the orifice shape and dimensions upon the flow physics of the jet, including the process of vortex formation and propagation. For instance, Utturkar et al. [21] reported that depending upon orifice shape, aspect ratio and curvature, the attainment of a threshold Strouhal

* Corresponding author.
*E-mail address:* akarn@ddn.upes.ac.in (A. Karn).

https://doi.org/10.1016/j.expthermflusci.2019.01.020
Received 13 October 2018; Received in revised form 23 December 2018; Accepted 16 January 2019
Available online 17 January 2019

**Nomenclature**

| | |
|---|---|
| $A_O$ | orifice cross-sectional area |
| $B$ | breadth of orifice |
| $d_c$ | distance between counter rotating vortices of vortex ring |
| $D_{ca}$ | cavity inner diameter |
| $D_{cy}$ | diaphragm disk diameter |
| $D_h$ | hydraulic diameter |
| $f$ | actuation frequency |
| $h$ | thickness of orifice plate |
| $H$ | cavity height |
| $L$ | slug length |
| $R_e$ | Reynolds number |
| $S_t$ | Strouhal number |
| $t$ | time |
| $T$ | time period of actuation cycle |
| $U_f$ | front end velocity of vortex ring calculated from sequence of LIF images |
| $U_r$ | velocity of counter rotating vortices in LIF images calculated from LIF images |
| $U_{avg}$ | time average velocity |
| $U_c$ | maximum velocity of time averaged velocities measured in transverse direction at any streamwise location |
| $U_o$ | average velocity calculated from Slug length divided by half of actuation period |
| $V_s$ | slug volume |
| $V_D$ | volume of fluid displaced by diaphragm |
| $W$ | width of orifice |
| $X, Y, Z$ | co-ordinate directions |
| $\Delta$ | diaphragm displacement |

number is required for vortex formation and propagation. Ai et al. [18] conducted an experiment on continuous jets from a circular and square nozzle having equal momentum flux and concluded that compared to circular continuous jets, square jets penetrate less due to enhanced entrainment and higher mixing efficiency. Similarly, Chaudhari et al. [6] reported that at lower axial distance from the synthetic jet exit, a rectangular orifice with the same hydraulic diameter as a square and circular orifice gives higher heat transfer coefficient than an orifice with square or circular cross-section. Watson et al. [22] compared the vortex rings produced by circular and rectangular orifices having constant area and reported that the synthetic jet produced by rectangular orifice is more likely to become turbulent than a circular one, even though the peak exit velocity is same for both the jets. The reason behind such a behavior is primarily attributed to the small-scale mixing near the four

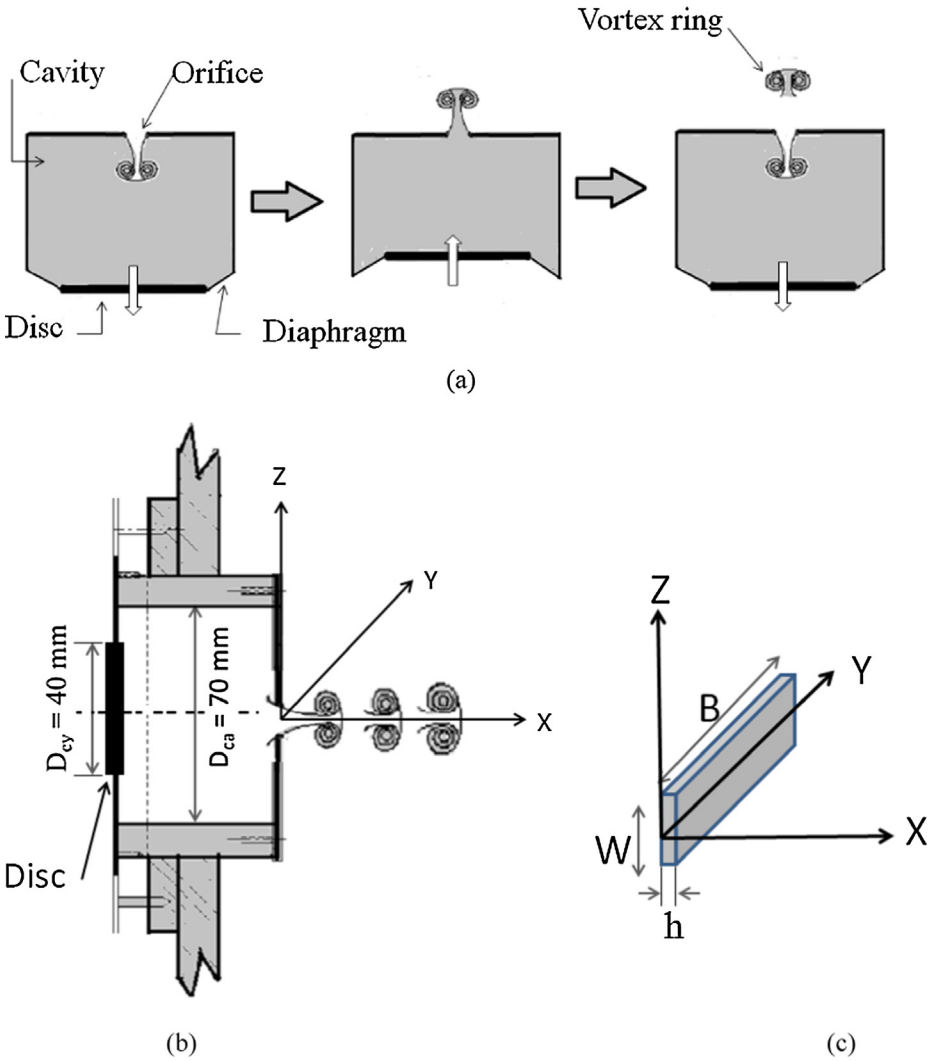


**Fig. 1.** (a) Schematic showing the synthetic jet operation, (b) cross-sectional view of the cavity, orifice and synthetic jet in XZ-plane and (c) details of co-ordinate notation and the orifice geometry.

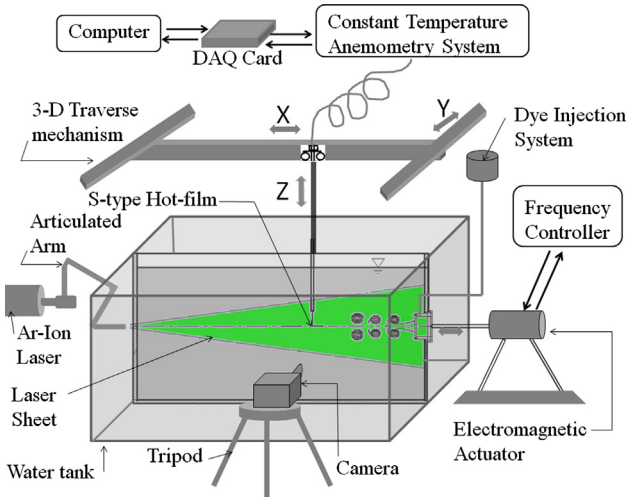


**Fig. 2.** Experimental set-up for flow visualization and velocity measurement of synthetic jet in quiescent condition.

corners of a rectangular orifice. Thus, the flow physics in the case of a rectangular orifice is significantly different as compared to a jet with a circular or a square cross-section. One of such interesting phenomenon, that clearly differentiates a rectangular orifice compared to circular geometry, is the phenomenon of axial switching of vortex rings. In the axial switching of a noncircular jet, the major axis of vortex ring undergoes axial contraction while minor axis experiences axial stretching [23]. The vortex ring undergoes many changes in its shape prior to axial switching depending on the ratio of the major to minor axis. The regions of the vortex ring with higher curvature convect ahead of the rest due to higher local induced velocity. Due to stretching, the corner portion comes towards the center, which in turn pushes the slower side outward increasing its curvature. Consequently, the major axis becomes minor, minor axis becomes major, and this switching is repeated as the vortex convects downstream until its breakdown. Hussain et al. [14] explained this axial switching for excited and non-excited elliptical continuous jet based on difference in velocities of different segments of vortex ring. The non-circular vortex ring having curvature dependent self-advection velocity produces stronger three-dimensional deformation compared to the circular counterpart. The flow dynamics behind the axial switching of a rectangular pulsed jet was also studied by IiO et al. [15], where it was shown that the shorter sides of the vortices move faster towards the jet axis than the longer side, while the vortices formed at the longer side moves away from the jet axis increasing the curvature further, resulting in axial switching.

Apart from the axial switching of vortex rings, another interesting phenomenon of vortex splitting, also known as bifurcation has been reported for rectangular shape vortex rings [5]. They focused on studying the formation of a single vortex ring in two different ways: a single forward stroke followed by a backward stroke and a forward stroke without a backward stroke. For a range of piston velocity profiles and stroke lengths, they reported the non-splitting of primary vortex and the bifurcation of vortex rings, respectively for the two cases. Therefore, it is the occurrence of the backward stroke that has a predominant effect on the splitting of the vortex rings. Since, the synthetic jet is also a cyclic repetition of forward and backward strokes, a periodic recurrence of the bifurcation phenomenon is not expected to occur. Although the bifurcation of a single vortex or a plain jet has been reported in the prior literature, however, the wake physics of a single vortex is substantially different as compared to a train of vortex rings in a synthetic jet. To the authors' best knowledge, no prior study conducted on the flow physics of synthetic jets has ever reported the occurrence of vortex bifurcation and explained the underlying physics for a range of frequencies or for different aspect ratios of rectangular orifices. Further, there have been very few investigations of vortex structures and quantitative characterization of synthetic jet behavior as a function of orifice aspect ratio, although it is amply evidenced by the existing literature that the nozzle shapes of both the continuous and synthetic rectangular jets play an important role in the jet evolution downstream. Thus, the present study aims at the investigation of synthetic jets generated using rectangular shape orifice having various aspect ratios using Laser Induced Fluorescence (LIF) and Constant Temperature Anemometry (CTA) technique. We report the jet formation and near field behavior of synthetic jet due to change in aspect ratio and actuation frequency. Finally, by narrowing down in a specific range of operating parameters, we also report the occurrence of a unique phenomenon of bifurcation of synthetic jets, which has hitherto not been reported, to the authors' best knowledge.

## 2. Experimental setup and methodology

The schematic of the synthetic jet actuator used in this study is shown in Fig. 1a–c. It comprises of a cylindrical cavity made of acrylic, having flexible convolute type diaphragm of neoprene rubber at one end, with the orifice at the other end. The inner diameter of cavity ($D_{ca}$) and the height are 70 mm and 60 mm, respectively. A circular steel disc of diameter 40 mm ($D_{cy}$) and 3 mm thickness is fixed at the center of diaphragm, and is connected to the electromagnetic actuator through a steel rod. The actuator is made to oscillate sinusoidally using a voltage input that is generated by a frequency controller unit. At the other end of the cavity, a provision has been made to mount the orifice plates.

A water tank of dimensions 1000 × 500 × 500 mm$^3$ made of 12 mm thick acrylic sheet has been employed to provide full optical access from all sides, for the purpose of visualization and characterization of the synthetic jet. The actuator is placed at the center of 500 × 500 mm$^2$ sidewall, such that the synthetic jet is located at an identical distance of 250 mm from the bottom wall as well as the free surface of water. An orifice size of 12 mm (hydraulic diameter) has been used, yielding a value of the ratio of the diameter to edge length of the tank as 0.024. The resulting low blockage ratio of 2.4% suggests that there is negligible effect of the wall or the free surface on the synthetic jets in our experiments. A Schematic of the experimental set-up is shown in Fig. 2. As shown in Fig. 2, the velocity measurements are carried out using a single hot-film probe (TSI 1212-20W), connected to a constant temperature anemometry system (TSI, Model No: IFA 300). A T-type thermocouple is mounted inside water and connected to the

**Table 1**
Details of synthetic jet actuator actuation conditions i.e. frequency and displacement with corresponding dimensionless number (*Re, St,* and $L/D_h$) for various orifice sizes.

| Orifice size | AR1 (12 × 12 mm$^2$) | | | | AR2 (9 × 18 mm$^2$) | | | | AR4 (7.5 × 30 mm$^2$) | | | |
|---|---|---|---|---|---|---|---|---|---|---|---|---|
| $f$ (Hz) | 1.05 | 1.65 | 4.06 | 5.96 | 1.05 | 1.65 | 4.06 | 5.96 | 1.05 | 1.65 | 4.06 | 5.96 |
| Δ (mm) | 1.11 | 1.58 | 2.24 | 3.15 | 1.11 | 1.58 | 2.24 | 3.15 | 1.11 | 1.58 | 2.24 | 3.15 |
| $V_d$ (mm$^3$) | 2845 | 4021 | 5710 | 8041 | 2845 | 4021 | 5710 | 8041 | 2845 | 4021 | 5710 | 8041 |
| *Re* | 242 | 553 | 1742 | 3864 | 215 | 491 | 1549 | 3435 | 155 | 354 | 1115 | 2473 |
| *St* | 0.61 | 0.43 | 0.30 | 0.22 | 0.68 | 0.48 | 0.34 | 0.25 | 0.95 | 0.67 | 0.47 | 0.34 |
| *Fn* (=$L/D_h$) | 1.6 | 2.3 | 3.3 | 4.5 | 1.5 | 2.1 | 2.9 | 4.0 | 1.1 | 1.5 | 2.1 | 2.9 |

anemometry system for temperature correction. The data acquisition is carried out using THERMAL-PRO software and LABVIEW program is used for post-processing the data. The hot-film probe is mounted on a three-dimensional (3D) traverse to facilitate accurate measurements using hot-film in all three (X, Y and Z) directions.

For the visualization of flow, Laser Induced Fluorescence (LIF) technique has been used. A COHERENT® INNOVA-90 4W continuous Ar-Ion Laser has been employed for illumination. A concave cylindrical lens of focal length 25 mm mounted in front of the laser light source, generates a laser sheet of 1.5 mm thickness. The LIF images (in the XZ-plane) are captured at 30 fps with a resolution of 600 × 1280 pixels using a Basler ® A 501 KC CMOS camera. The laser sheet aligned along the central plane of the orifice, perpendicular to the orifice plate is used for visualization of the synthetic jet created downstream. Concentrated solution of Fluorescein sodium [$C_{20}H_{10}Na_2O_5$] is used for LIF visualization and it is pumped into the cavity through the small dye ports attached to the cavity of synthetic jet actuator. Frequency is measured using a hot-film probe, located at the center of the jet exit across a range of experimental conditions that are presented in Table 1. The Reynolds number (*Re*), Strouhal number (*St*) and Formation number, *Fn* ($Fn = L/D_h$) based on average jet exit velocity ($U_0$) and hydraulic diameter ($D_h$) are also tabulated. The Formation number, or normalized stroke length $L/D_h$ ratio represents the combined effect of these parameters on vortex formation process and its propagation in the downstream direction. For sinusoidal oscillation of diaphragm, the volume $V_D$ is estimated using cavity inner diameter ($D_{ca}$), disk diameter ($D_{cy}$) and amplitude of oscillation (Δ) [19]. An accelerometer has been used for measuring the amplitude of oscillation. Using incompressible parallel flow assumption, slug length (*L*) for synthetic jet is calculated as the ratio of slug volume ($V_S$) of fluid driven out through the orifice in forward stroke of diaphragm and cross-sectional area of orifice ($A_0 = BW$), where *B* and *W* is breadth and width respectively. Since for an incompressible flow, slug volume and volume displaced by diaphragm are same, so using Eqs. (i) and (ii), slug length can easily be calculated. The mathematical representations for these calculations are as follows:

$$V_d = \frac{\pi\Delta}{8}(D_{ca}^2 + D_{cy}^2) \quad \text{(i)}$$

$$V_S = A_O L \quad \text{(ii)}$$

$$L = \frac{V_D}{A_o} \quad \text{(iii)}$$

Further, the averaged jet exit velocity ($U_o$) can be calculated based on the actuation frequency and the slug length, as

$$U_o = 2fL \quad \text{(iv)}$$

Finally, the Reynolds number and Strouhal number are defined conventionally based on actuation frequency, averaged jet-exit velocity, hydraulic diameter and kinematic viscosity as

$$Re = \frac{U_o D_h}{\nu} \quad \text{(v)}$$

$$S_t = fD_h/U_o \quad \text{(vi)}$$

The overall uncertainties in velocity measurement using the hot-film are due to the combined effects of both calibration and velocity reduction. The effects of variations in ambient pressure and temperature are considered negligible and thus ignored in the calculation of calibration uncertainty. The total uncertainty in velocity measurement obtained using hot-film is then found to be ± 4.1% of the actual velocity. The uncertainty in both the fluid volume ejection and the formation number ($L/D_h$) is calculated to be ± 3.6%. The Reynolds number is calculated using the averaged velocity of fluid during ejection period as given in Eq. (v). The uncertainty in averaged jet exit velocity ($U_o$) depends on volume of ejected fluid in forward stroke, frequency of actuation, and hydraulic diameter. The exact frequency imposed on diaphragm is measured by the oscilloscope and is compared with the frequency obtained from velocity signal outside the suction zone. The maximum difference between the two is found to be less than 0.05 Hz.

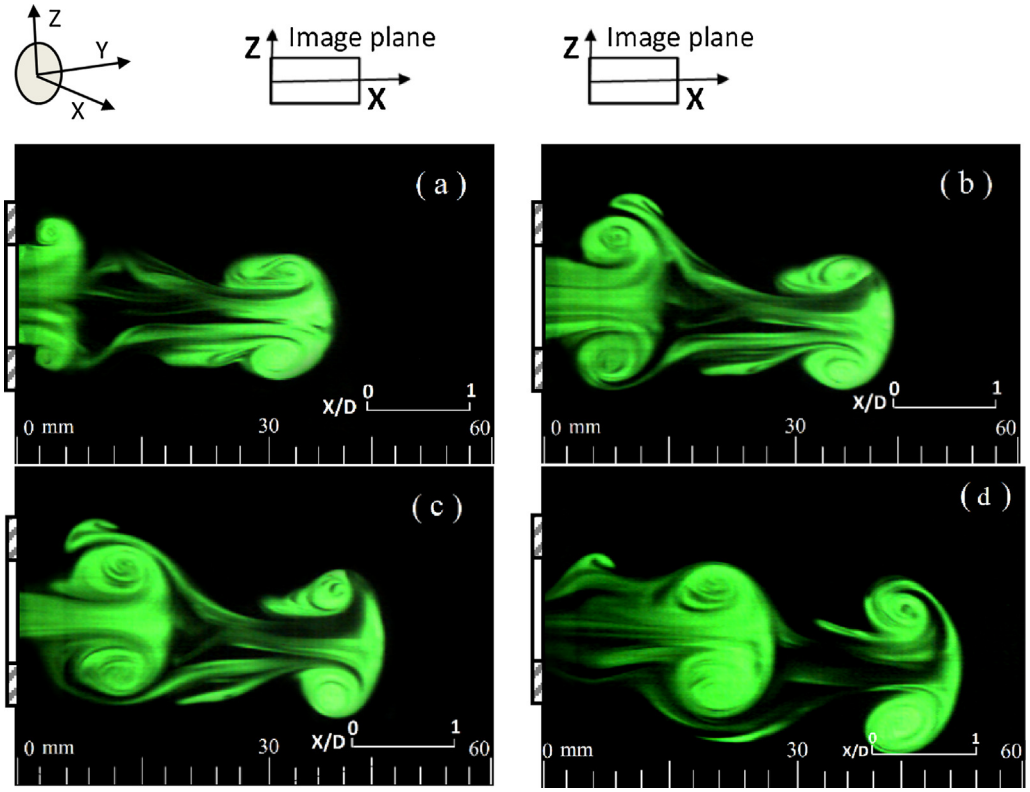


**Fig. 3.** Flow visualization images of synthetic jet in XZ-plane for a circular orifice of diameter D = 12 mm at $f$ = 1 Hz during four different time steps: (a) t ~ T/4, (b) t ~ 2 T/4, (c) t ~ 3 T/4 and (d) t ~ 4 T/4, where T is the time period of cycle at $L/D_h$ = 2.03 and $Re$ = 307.

Neglecting the variation in kinematic viscosity of water, the uncertainty in the calculation of Reynolds number is found to be 3.67%. An uncertainty range of 6.2–12.6% has been found in the measurement of the separation distance between the counter rotating vortex core in LIF images for the range of actuation frequency in the present study. The least count of the 3D traverse is 0.01 mm in all the directions, thus giving an uncertainty in spatial measurement to be 0.01 mm. Further, for the sake of brevity, actuation frequency of 1 Hz and 2 Hz are referred to as 'lower' frequencies, whereas 4 Hz and 6 Hz are alternatively referred to as 'higher/greater frequencies', respectively hereafter.

## 3. Results and discussions

The formation of vortex ring in synthetic jet depends on various parameters such as actuation frequency, amplitude of oscillation, shape, thickness of orifice, cavity geometry etc. It is worth noting here that in our experiments, the frequency and the diaphragm amplitude of the electromagnetic actuator are coupled with each other, still yielding a constant liquid mass flux out of the orifice at a particular frequency. Since it is not possible to extricate the effect of variation in either $f$ or $\Delta$ independent of each other, the volumetric displacement $V_D$ is kept fixed for a particular frequency for all orifice shapes. Thus, the comparisons across different orifices are made at identical $V_D$ for all the orifices. Yet, to facilitate comparisons with the previous reported results, we comply with the notation followed in the prior literature and thus report our findings with respect to the actuation frequency, although the corresponding $V_D$ can be noted from Table 1. Since the current study aims to characterize the flow field and study the vortex behavior at various aspect ratios of the rectangular orifice, other parameters such as the hydraulic diameter, actuation frequency and displacement of diaphragm are kept constant. The characteristics of synthetic jet for different orifice aspect ratios as a function of actuation frequency are studied using LIF visualizations, velocity time trace and power spectral density of velocity signals, and are reported in the following sections.

### 3.1. LIF visualization

LIF visualization is employed to study the structure of the vortex rings generated by the synthetic jet. Before carrying out the experiments of the synthetic jet with rectangular orifice, experiments are carried out with the much-reported circular orifices, in order to test the concurrence of our results with the prior literature. In addition, these experiments are also conducted to validate the capability of our experimental setup and measurements to accurately capture the flow physics of the synthetic jet, as reported by the prior studies.

#### 3.1.1. Validation with respect to other experimental results

A time sequence of LIF images for approximately one complete actuation cycle is presented in Fig. 3 to show the evolution of vortex ring for a circular orifice. The figure clearly shows the formation of initial vortex ring and its subsequent advection downstream, for the formation number based on slug length varying in the range of 1.1–4.5 for all three aspect ratios. In our experiments, the calculated non-dimensional numbers *Re, St* and *Fn* are kept the same as those used by Jabbal et al. [16] for the diaphragm actuation system, ensuring that these non-dimensional parameters actually capture the physics of vortex formation. The flow structures obtained at $L/D_h = 2.03$ and $Re = 307$ indeed closely match with that reported by Jabbal et al. [16], and are in perfect congruence with the reports of Gharib et al. [10] and Crook and Wood [7] as well. According to Gharib et al. [10], circular vortex ring grows to its maximum size from circular nozzle generated using piston cylinder actuation mechanism in the range of $L/D_h = 2–14.5$ and Reynolds number of 2300–6000. The apparent difference between the *Re* values in the current work vis-à-vis that of

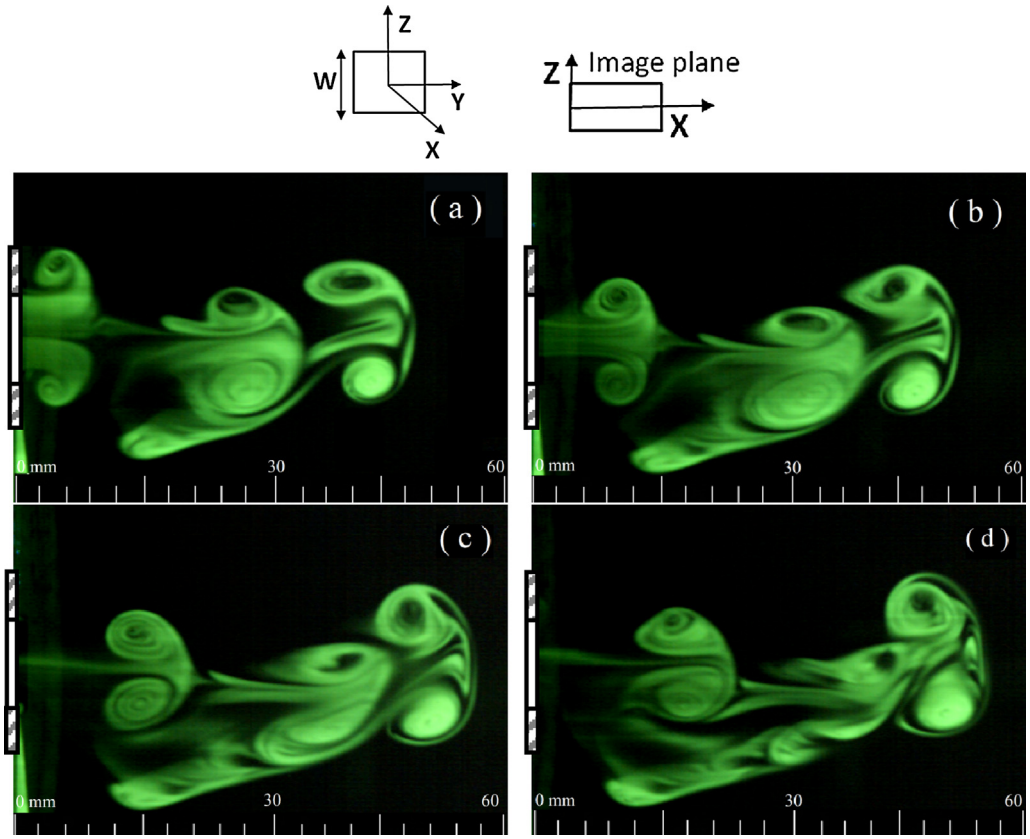


**Fig. 4.** Flow visualization images of synthetic jet in XZ-plane for rectangular orifice AR1 orifice case, hydraulic diameter $D_h = 12$ mm at $f = 1$ Hz during four different time steps: (a) t ~ T/4, (b) t ~ 2 T/4, (c) t ~ 3 T/4 and (d) t ~ 4 T/4, where T is the time period of cycle at $L/D_h = 1.61$ and $Re = 242$.

Gharib et al. [10] can be attributed to the different ways *Re* is defined in the two studies. Contrary to the current study, *Re* has been defined equal to $\Gamma/\nu$ in the work of Gharib et al. [10] on vortex rings. Similar pattern of synthetic jet flow structures has also been reported by Crook and Wood [7] for circular orifice in the range $L/D_h$ = 2–10 and *Re* = 330–2300.

*3.1.2. Near-region vortex formation and evolution for different orifice aspect ratios*

It should be noted here that *Fn* alone is not sufficient to determine

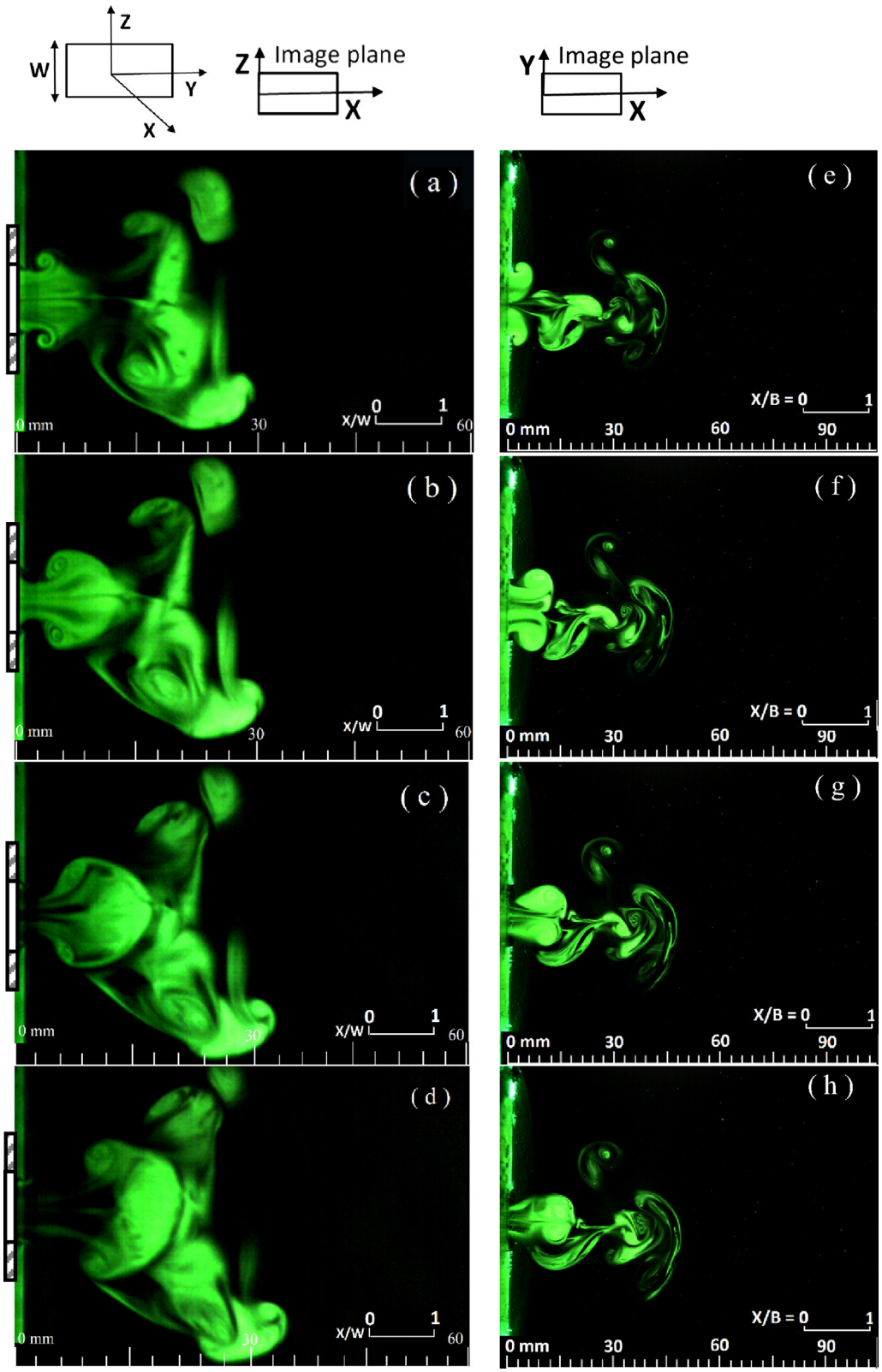


**Fig. 5.** Flow visualization images of synthetic jet in XZ and XY-plane from rectangular orifice, AR2 aspect ratio case, hydraulic diameter $D_h$ = 12 mm at $f$ = 1 Hz during four different time steps: (a, e) t ~ T/4, (b, f) t ~ 2 T/4, (c, g) t ~ 3 T/4 and (d, h) t ~ 4 T/4, where T is the time period of cycle at $L/D_h$ = 1.5 and *Re* = 215.

the flow characteristics of a non-circular synthetic jet. The presence of corners in a rectangular orifice and its aspect ratio also plays an important role in the formation and propagation of vortex rings. Figs. 4–6 show the evolution of vortex ring at $f = 1$ Hz for the three aspect ratios of 1, 2 and 4, respectively at four different time instants within one complete cycle. As evident from these figures, the size of the vortex ring formed close to the orifice exit at t ~ T/4 in Fig. 4(a) is slightly larger than the size of the subsequent vortex rings generated in a particular

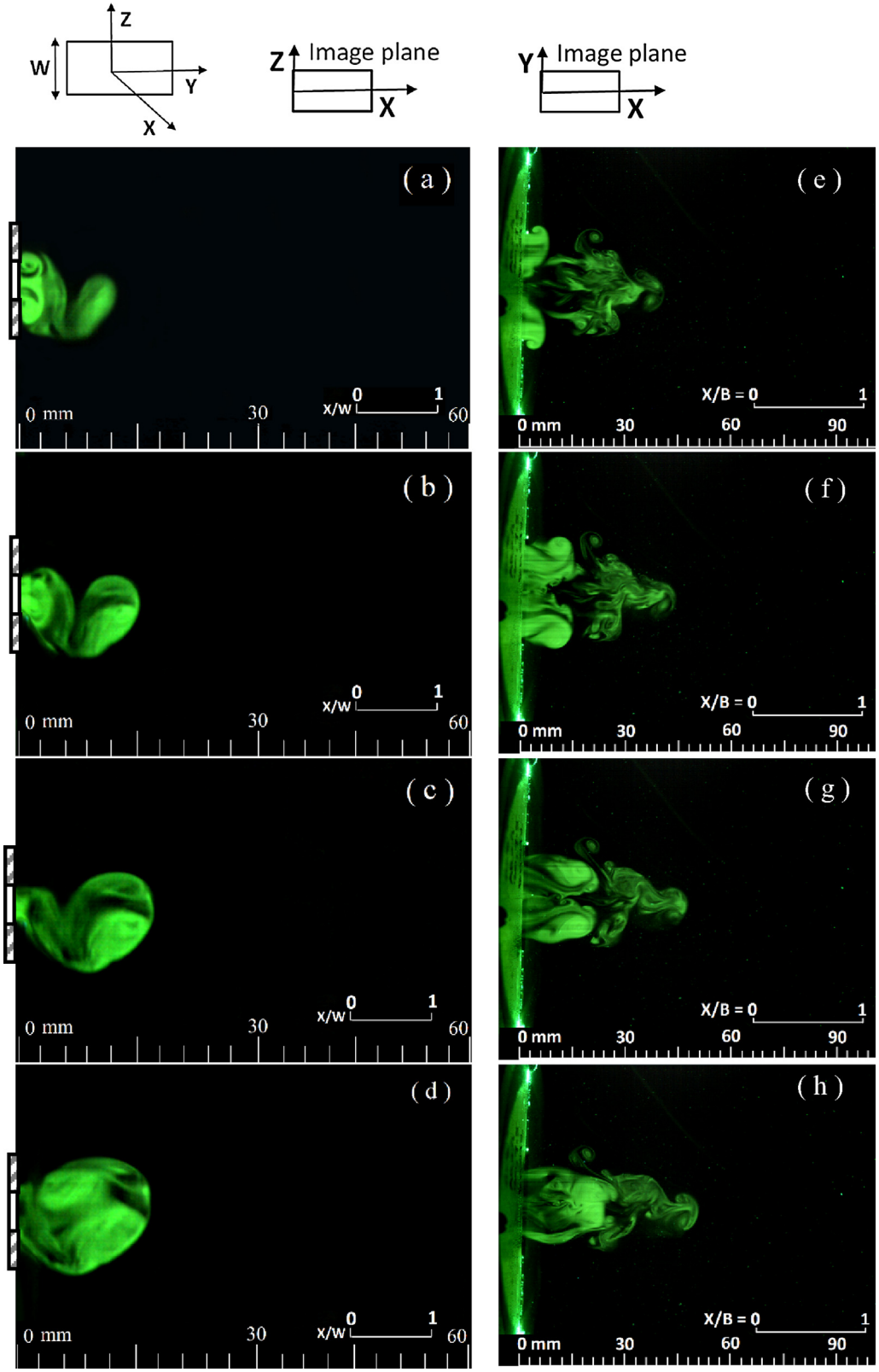


**Fig. 6.** Flow visualization images of synthetic jet in XZ and XY-plane from rectangular orifice, AR4 aspect ratio case, hydraulic diameter $D_h = 12$ mm at actuation frequency, $f = 1$ Hz during four different time steps: (a, e) t ~ T/4, (b, f) t ~ 2 T/4, (c, g) t ~ 3 T/4 and (d, h) t ~ 4 T/4, where T is the time period of cycle at $L/D_h = 1.1$ and $Re = 155$. (*Images in both the planes are not acquired at the same instant of time).

cycle. Once the vortex rings detach itself from the orifice exit and propagate downstream, it shrinks in size, a phenomenon reported as 'overshoot' of the vortex ring [18]. Another significant observation is the pairing of two subsequent vortex in the downstream. As the vortex loses its strength causing a reduction in its self-induced velocity, the preceding vortex having higher induced velocity from the next cycle approaches the slow moving vortex and merges with it, as it can be observed from Fig. 4(c) and (d). A single vortex ring splits itself into two isolated vortex rings in the XZ-plane and advects at an angle to each other for the AR2 orifice as illustrated in Fig. 5 at $f = 1$ Hz. However, the counter rotating vortices in XY-plane moves towards the jet centerline and at the downstream location where these merge, the vortex ring splits in XZ-plane. The sequence of LIF images reveals that the convection velocity difference between the front end of vortex ring ($U_f$) and the peripheral ring velocity ($U_r$) is of significant importance in the bifurcation of the vortex rings. The velocity difference between $U_f$ and $U_r$ is calculated using the sequence of LIF images. For AR = 4 and $f = 1$ Hz, a portion of ejected vorticity is sucked back inside the cavity while the portion of the vortex ring on the shorter side of the orifice moves towards the center of the vortex ring (Fig. 6). The approximate time duration between each frame is obtained using frame grabbing rate and thus corresponding velocity is calculated.

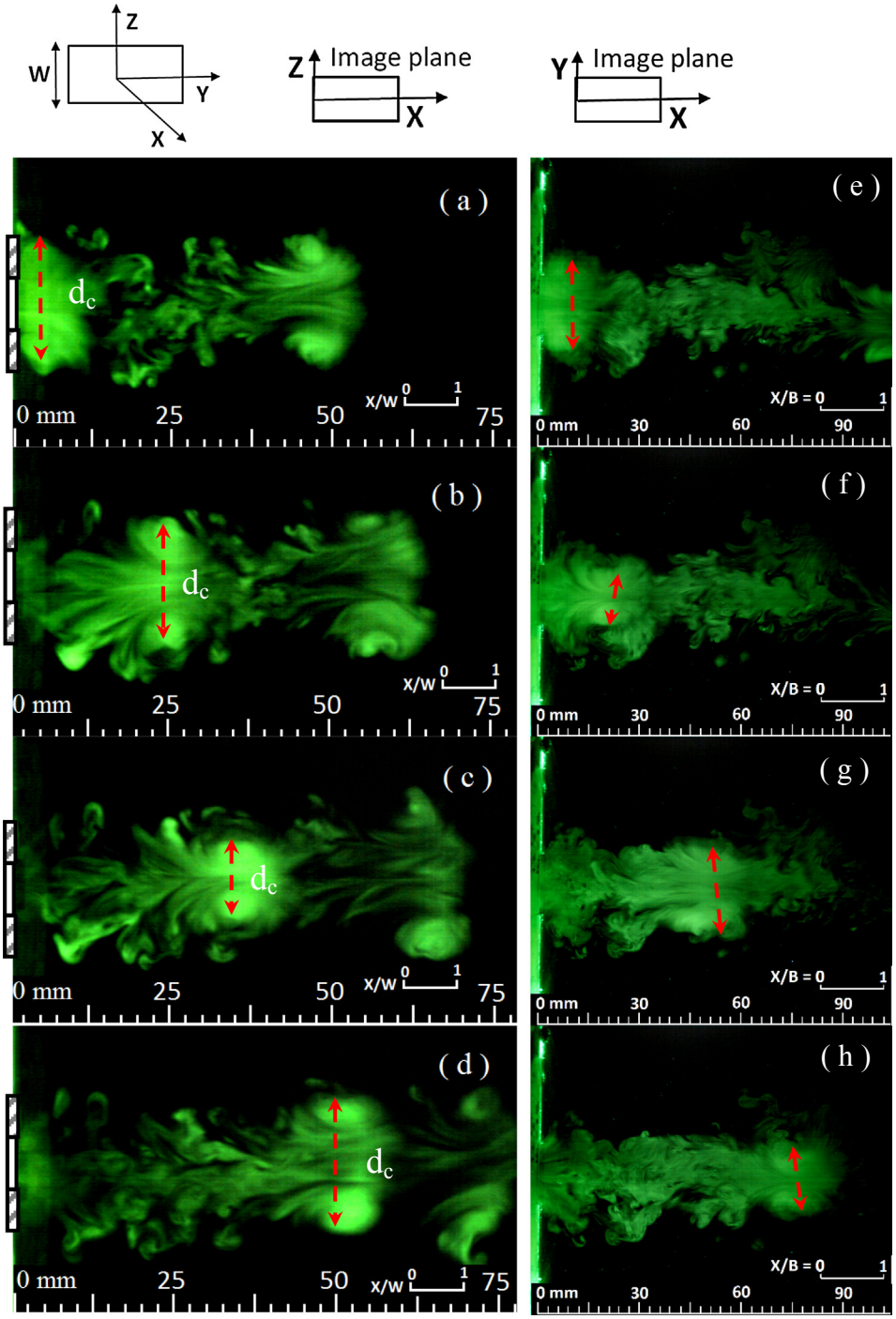


**Fig. 7.** Flow visualization images of synthetic jet in XZ and XY-plane from rectangular orifice, AR2 aspect ratio case, hydraulic diameter $D_h = 12$ mm at actuation frequency, $f = 4$ Hz during four different time steps: (a, e) t ~ T/4, (b, f) t ~ 2 T/4, (c, g) t ~ 3 T/4 and (d, h) t ~ 4 T/4, where T is the time period of cycle at $L/D_h = 3.3$ and $Re = 1742$. (*Images in both the planes are not acquired at the same instant of time).

Fig. 7 shows the sequence of LIF images for AR2 orifice at an increased actuation frequency (f = 4 Hz). After certain distance downstream, the distance between two counter rotating vortices of vortex ring is found to increase and decrease subsequently in both the orthogonal planes XZ and XY. In the time interval between t ~ 2 T/4 and t ~ 3 T/4, the distance between the two counter rotating vortices of vortex ring decreases in XZ-plane and increases in XY-plane confirming the phenomena of first axial switching. The distance between counter rotating vortices increases between t ~ 3 T/4 and t ~ 4 T/4 in XZ-plane and decreases in XY-plane, confirming the second axial switching of vortex ring.

The combined effect of frequency and aspect ratio has been shown for all the three orifices in Fig. 8. At a low *Re*, the propagation velocity of newly formed vortex rings is quite low and the vortex shape is extensively governed by the suction period of following cycle causing a wide variation of flow patterns. A weak trailing jet with a distinct leading vortex ring is observed for an aspect ratio of unity (AR1) at $f = 1$ Hz. Upon traveling a certain streamwise distance, it merges with the following vortex ring and the flow pattern changes from laminar to chaotic or probably turbulent with increase in frequency leading to a stronger trailing jet. The vortices emanating from rectangular orifice AR2 are observed to be bifurcated at lower actuation frequencies. Vortex ring splits into two halves forming two small vortex rings, both moving at same speed with an angle to each other. At this aspect ratio, the vortex ring sheds a strong trailing jet and the flow becomes even more complex at greater frequencies. The synthetic jet for AR4 orifice at greater actuation frequencies breaks into small pieces in their early stage of the vortex formation and thus no recognizable vortex ring is observed in LIF images. The spreading and mixing of synthetic jet is quite high for AR4 orifice as compared to AR1 and AR2 orifices in the near field region. This may be due to partial suction of the ejected fluid and influence of instability in the corners. The flow patterns at this aspect ratio are highly unstable leading to a greater rate of fluid entrainment.

As the axial switching of vortex rings has a substantial impact on the fluid entrainment and the resulting flow structures, the number of its occurrence before the breakdown of vortex ring is also worth investigating. The separation distance between the counter rotating vortices increases and decreases with time. The contraction of vortex ring in XY-plane towards the synthetic jet centerline decreases the separation distance between them. The movement of the vortex ring towards the center in XY-plane pushes the vortex tube outwards in Z-direction and thus an increment in separation distance between the counter rotating vortices is observed in the XZ-plane. Fig. 10 shows minor variations in the separation distance of counter rotating vortices in the downstream direction in XY and XZ-planes, which indicates that either the axial switching is absent or two orthogonal planes are not sufficient to capture the event. This point can be further substantiated by the prior studies on synthetic jets that have reported a 45 degree of axial switching for square shaped vortex rings [12], or have asserted that the continuous square jet is not expected to have any axial switching when the ratio of circular-equivalent diameter to momentum thickness at the side of the orifice is small [13].

It is evident form LIF images in Fig. 8(e) and (f) and the convection velocity of vortex segments ($U_f$ and $U_r$) in Fig. 9, that the vortex rings splits into two halves due to a large difference between the magnitudes of $U_f$ and $U_r$, and the longer time lag for their velocities to approach each other, for the AR2 orifice case at $f = 1$ and 2 Hz. The splitting of vortex ring is not observed for orifices that generate vortices having small, negligible or equal difference between $U_f$ and $U_r$ after the ejection period (t/T > 0.5). The variation in $U_f$ and $U_r$ for AR1 and AR2 orifice cases at four different frequencies (1, 2, 4, 6 Hz) is further shown in Fig. 9. At $f = 2$, 4 and 6 Hz, due to early breakdown of vortex rings, the front-end velocity or ring velocity is indistinguishable. Initially the magnitude of $U_f$ is larger than $U_r$ between t/T = 0.1–0.5 for AR1 at $f = 1$ Hz (see Fig. 9(b)). The magnitude of $U_f$ and $U_r$ approach each

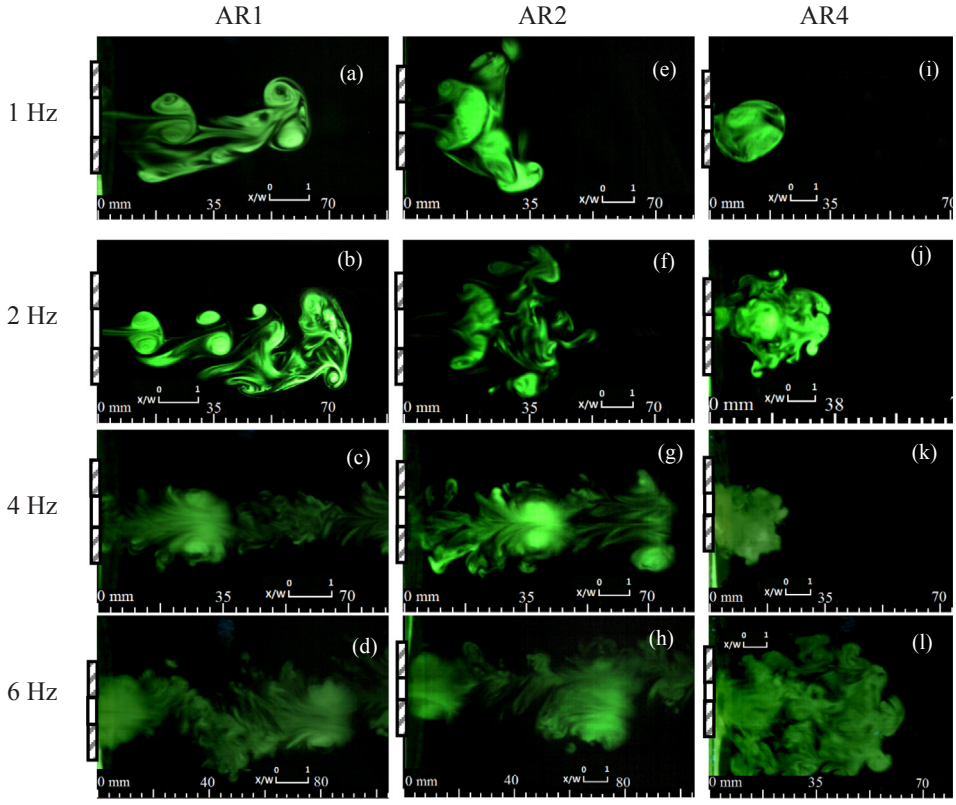


**Fig. 8.** Comparison of LIF images of (a–d) orifice AR1, (e–h) orifice AR2 and (i–l) orifice AR4 at an actuation frequency equal to (a, e and i) 1 Hz, (b, f and j) 2 Hz, (c, g, k) 4 Hz and (d, h, l) 6 Hz.

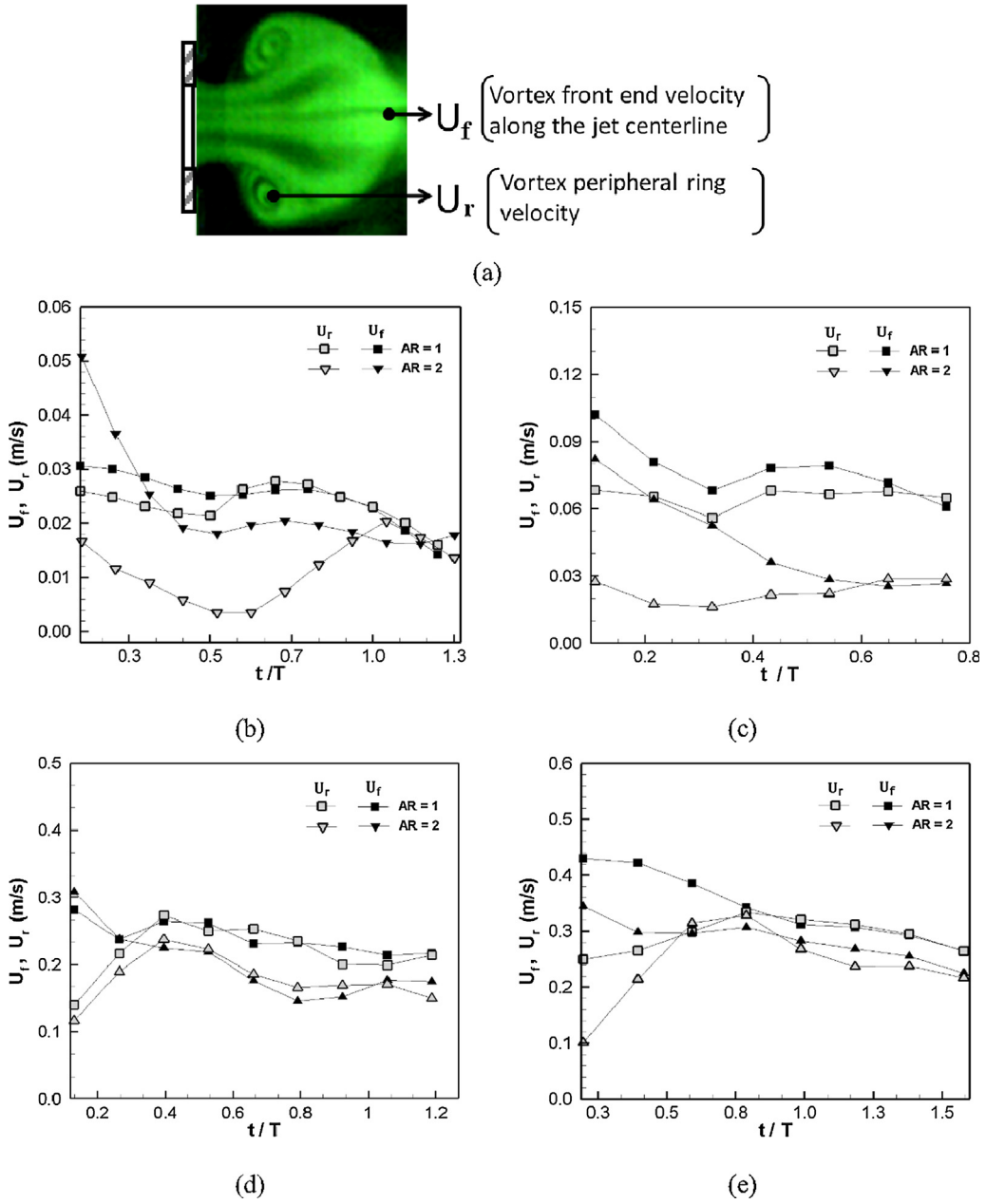


**Fig. 9.** Stream wise velocity $U_f$ (solid symbols) of front end of leading vortex ring and stream wise velocity $U_r$ (hollow symbols) of counter rotating vortices of vortex ring measured from the sequence of LIF images for AR1 and AR2 orifice cases at $f$ = (b) 1 Hz, (c) 2 Hz, (d) 4 Hz and (e) 6 Hz.

other after t/T = 0.5, but begins to differ again at t/T = 0.6 only to converge again at t/T = 0.9. After t/T = 0.9, the line of $U_f$ and $U_r$ separates again and proceed further with marginal space in between. The variation in the magnitude of $U_f$ and $U_r$ corresponds to the increase and decrease in self-induced velocity of shorter and longer side of vortex ring during axial switching. The vortex ring ejected from rectangular shaped orifice AR2 shows a larger difference between $U_f$ and $U_r$ and for longer duration (t/T = 0.1–1.0) in comparison to the AR1 orifice. This stretches the vortex ring in XZ-plane leading to vortex bifurcation. Similar trend with reduced magnitude is observed in Fig. 9(c) for AR2 at $f$ = 2 Hz. The magnitude of $U_f$ and $U_r$ remains unaffected until t/T = 0.55, but later between t/T = 0.65 and 75, they approach each other gradually and ultimately flip. The trend of vortex bifurcation is also observed for this case (see Fig. 8f for AR2 orifice) with reduced splitting angle. In addition, the bifurcated vortex rings breaks quickly for this case which may be linked to the reduced disparity between $U_f$ and $U_r$ in comparison to AR2 orifice at $f$ = 1 Hz. The differences in magnitude of $U_f$ and $U_r$ in Fig. 9(d) and (e) for AR1 and AR2 are more significant before t/T = 0.4 and 0.8 for $f$ = 4 Hz and 6 Hz, respectively, following which there is a negligent difference between the two.

The separation distance between the counter rotating vortices is shown in Fig. 10(b) for AR2 orifice. The variation in the size of vortex ring follows entirely different trends for axial switching and bifurcation process. The separation distance between the center of counter rotating vortices measured from LIF images in XZ and XY planes ($H_W$ and $H_B$) crosses each other at $X/W$ = 0.6 and 0.8 for $f$ = 1 and 2 Hz, respectively. After the vortex overshoot ($X/W$ > 0.3), the value of $H_W$ remains constant between X/W = 0.3–1.5 for lower $f$. However, $H_B$ decreases rapidly within this region and finally disappears as the counter rotating vortices merge. After this location, the vortex ring splits in XZ-plane (see Fig. 5) and the magnitude of $H_W$ increases rapidly (after vortex-splitting $H_W$ is measured between the top and bottom vortices). At greater $f$, $H_B$ and $H_W$ flip their values twice and the vortex rings breaks halfway through the third switching event. The flipping of $H_W$

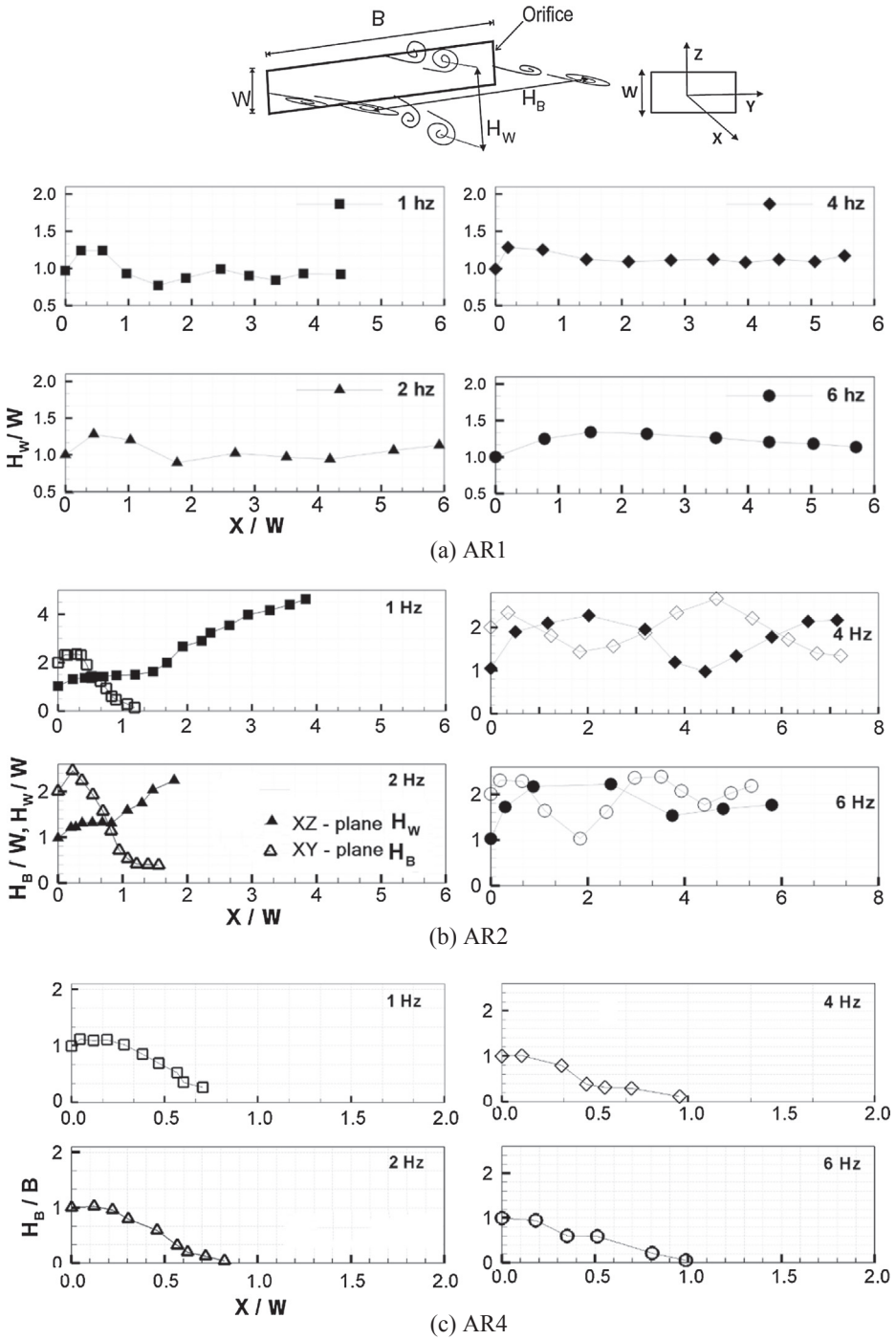


**Fig. 10.** Separation distance between the counter rotating vortices in LIF images captured in XY and XZ-plane at $f$ = 1, 2, 4 and 6 Hz for the orifice (a) AR1 (b) AR2 and (c) AR4.

and $H_B$ represents the completion of axial switching of vortex ring. At $f$ = 4 Hz, the first axial switching is completed near $X/W$ = 2 and the second axial switching between near $X/W$ = 4.4. The attempt of third axial switching is also observed between $X/W$ = 4.4–7 before vortex breakup. At 6 Hz, the low frame grabbing rate limits the exact identification of the locations of axial switching, but it is located between $X/W$ = 1.8–2.2 for first axial switching and between $X/W$ = 3.5–4 for second axial switching. The separation distance between the counter rotating vortices are difficult to measure from LIF images in XZ-plane for AR4 orifice due to early breakdown, mixing and chaotic flow in the region. Therefore, the separation distance ($H_B$) is measured only in XY-plane as shown in Fig. 10(c). At lower $f$, the magnitude of $H_B$ approaches to zero at $X/W$ = 0.65 and 0.85 respectively, whereas at greater $f$, $H_B$ approached to zero at $X/W$ = 1. The trend of variation for $H_B$ at greater $f$ for AR4 orifice is similar to the observation obtained for the bifurcation cases at lower $f$ for AR2 orifice. However, instead of splitting, the forming vortex ring transitions into tiny vortices close to the orifice that spread swiftly in the XZ-plane. The increased spreading in XY-plane is observed after $H_B$ is almost zero or negligible.

### 3.2. Velocity time trace

Fig. 11 presents four cases of flow patterns for different orifice aspect ratios and frequency, for which velocity time trace will be

(a) Vortex ring without a trailing jet or with a weak trailing jet




(b) vortex ring with strong trailing jet

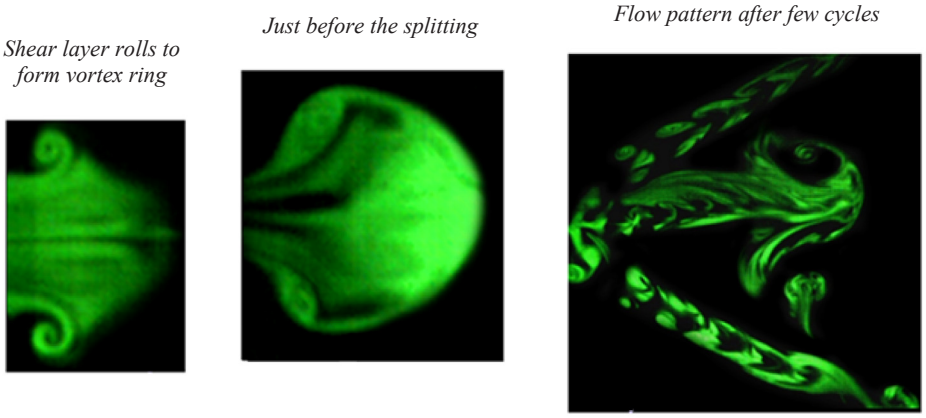


(c) Splitting of vortex ring

*Portion of the vortex ring ejected at center of orifice moving back inside the cavity due to following backward stroke*

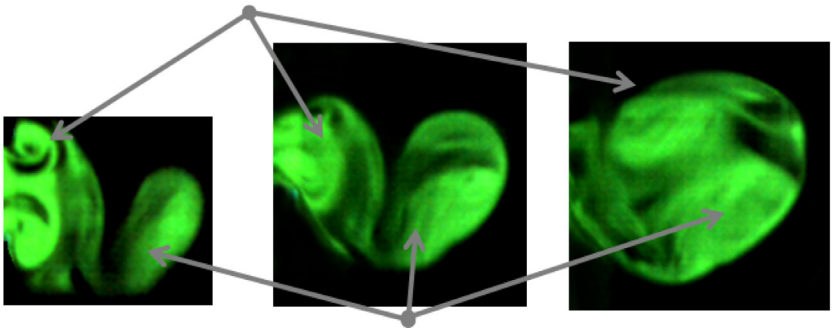

*Vortex ring ejected at shorter side of orifice moving towards the Synthetic jet centerline*

(d) Partial suction of ejected ring

**Fig. 11.** LIF images illustrating different synthetic jet evolution patterns of vortex ring: (a) AR1 at 1 Hz, (b) AR1 at 4 Hz, (c) AR2 at 1 Hz and (d) AR4 at 1 Hz.

considered in this section. As shown in Fig. 11a, a weak trailing jet with a distinct leading vortex ring is observed for an aspect ratio of unity (AR1) at $f = 1$ Hz. At a higher frequency of 4 Hz, the vortex ring upon traveling a certain streamwise distance merges with the following vortex ring and the flow pattern changes from laminar to chaotic or probably turbulent leading to a stronger trailing jet, as evident from Fig. 11b. The vortices emanating from rectangular orifice AR2 bifurcate at lower actuation frequencies, forming two small vortex rings, both moving at same speed with an angle to each other, as illustrated in Fig. 11c. The split vortex ring leaves behind a small fraction of vorticity portion of it, which moves slowly without forming a vortex ring leading to a ψ-shaped vortex pattern after few cycles. Finally, the synthetic jet for AR4 orifice at lower actuation frequencies may lead to partial suction of the ejected fluid as presented in Fig. 11d.

The velocity time trace at different downstream locations $X/W = 0$, 1, 2 and 3 for these four different cases, have been presented in Fig. 12. For a better comparison of pattern and strength of the velocity signal at various downstream locations, the signals are staggered but plotted on the same scale. The number of peaks present in the velocity signal determines the presence of suction stroke. For a given time period, the expected number of cycles or peaks are calculated by multiplying $f$ with time. When suction effects are present, the apparent peaks are more (approximately twice the expected) than the expected peaks near the orifice locations. The influence of suction stroke is present for all four cases at orifice exit as the number of peaks are approximately twice the expected number of peaks (see Fig. 12(a)). The duplication of peaks can be attributed to the directional insensitivity of hot-film, which leads to a false peak in velocity signal between two consecutive cycles. The suction and the ejection velocity are distinguished on the basis on vortex ring propagation in downstream direction, because for effective movement of the vortex ring in downstream direction, the time-averaged velocity during ejection period should be higher than the time-averaged velocity during suction period along the synthetic jet centerline. Further, at a downstream location, the suction effect decreases

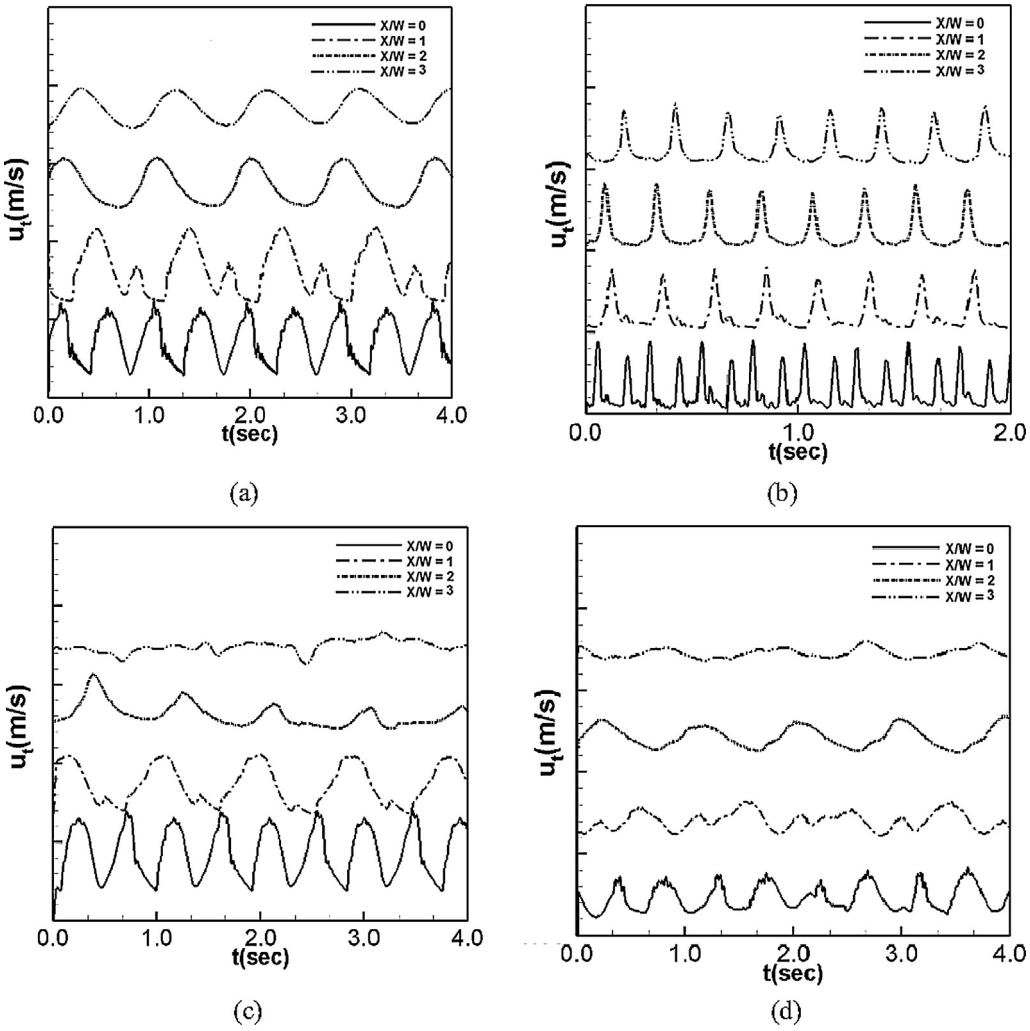


**Fig. 12.** Stream wise velocity signals (uncorrected) at $X/W$ = 0, 1, 2 and 3 along jet exit centerline for case (a) AR1, f = 1 Hz, (b) AR1, f = 4 Hz, (c) AR2, f = 1 Hz and (d) AR4, f = 1 Hz. For improving the clarity of presentation, the signals at different $X/W$ are displaced upwards with respect to each other.

and finally vanishes. The velocity signal for AR1, AR2 and AR4 orifice cases (Fig. 12(a), (c), (d)) are similar at $X/W = 0$ for $f = 1$ Hz. The velocity profile of suction and ejection stroke covers the full range of a cycle with nearly equal number of peaks and time-period for all aspect ratio at $f = 1$ Hz. However, the period of suction and ejection stroke is found to exist for AR1 at $f = 4$ Hz at $X/W = 0$ and the corresponding time-averaged velocity is seen to be lower.

Unlike ejection strokes, the suction period and its amplitude along the synthetic jet centerline decreases in a different way for all the cases at $X/W = 1$. The suction effect is found to be more pronounced for AR1 orifice than that of AR2 and AR4 orifice at $f = 1$ Hz. However, the suction effect is not present at this location for AR1 at $f = 4$ Hz. The propagation of isolated vortex ring along the jet centerline produces a distinct oscillation but shows a reduced amplitude as distance is increased from $X/W$ = 2–3 in Fig. 12(a). The number of peaks per second is equal to the actuation frequency and secondary peaks are negligible between $X/W$ = 0–1 indicating no suction effect after this location along the jet centerline for AR1 orifice at 4 Hz actuation in Fig. 12(b). Due to bifurcation of vortex ring for AR2 at 1 Hz, the velocity decreases rapidly along the jet centerline and is clear from signal trace at $X/W$ = 2–3 as shown in Fig. 12(c). The partial suction of ejected fluid and early breakdown of vortex ring decreases the velocity as seen in Fig. 12(d) at $f = 1$ Hz for AR4 orifice and consequently the amplitude of peaks decreases substantially.

### 3.3. Time-averaged velocity profiles

Figs. 13–15 show the mean streamwise velocity profile in X, Y and Z-directions at $f$ = 1, 2 and 6 Hz for aspect ratio of 1, 2 and 4 at $X/W$ = 1, 3, 5 and 10. A close examination of the velocity signals at various actuation frequencies and axial locations reveals that the suction velocity becomes negligible beyond $X/W = 3$ for all the cases studied. The average velocity in downstream direction is calculated by subtracting the suction velocity from the jet exit velocity for a maximum of 30 actuation cycles before $X/W = 3$. The average velocity profile including both suction and ejection velocity, measured using a hot film is presented below.

Figs. 13(a)–15(a) show the mean velocity variation along the synthetic jet centerline at different downstream locations at $f$ = 1, 2 and 6 Hz respectively for all the three orifices at all four downstream locations. As expected, the velocity distribution along the synthetic jet centerline for all three orifices at the lowest frequency are found to be different from each other. The average velocity for AR1 at $f = 1$ Hz initially increases in the downstream direction to a constant value which is followed by rapid reduction till $X/W = 7$ and decreases slowly with further increases in downstream distance. The velocity increases rapidly from the orifice exit as the shear layer ejected rolls to form the vortex rings, that move away from the orifice exit due to self-induced velocity upto certain streamwise distance before the next suction strokes begins. As the vortex ring propagates, it drags surrounding fluid

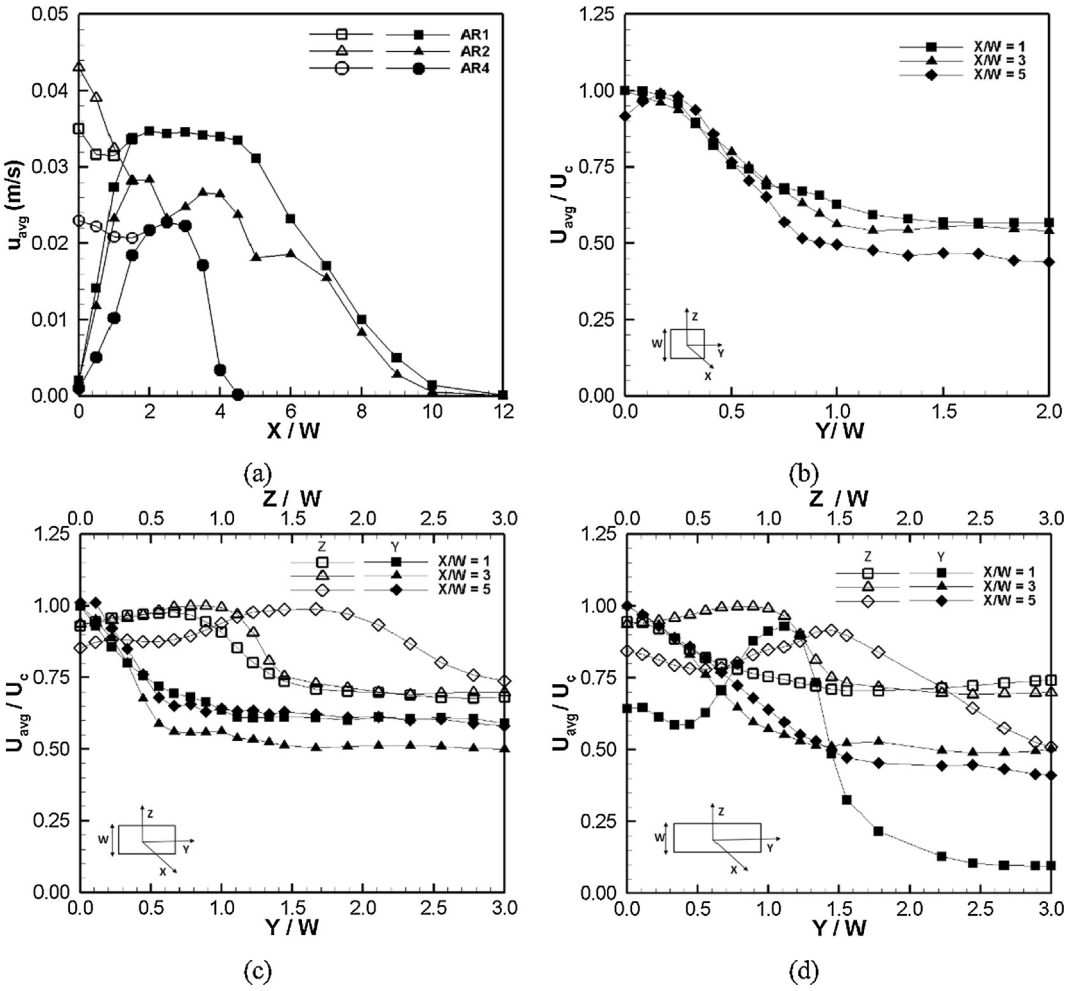


**Fig. 13.** (a) Time averaged mean stream wise velocity profile in X-direction at $f = 1$ Hz without correction of suction velocity (solid symbols) and with correction (hollow symbols) for different aspect ratio orifices. Normalized velocity profile at $f = 1$ Hz for (b) AR1 orifice in Y-direction, (c) AR2 and (d) AR4 orifice in Y and Z-direction at different downstream locations ($X/W$). Filled symbols represent Y-variations and hollow symbols represent Z-variations of velocity in (c) and (d).

along with it and increases its size with reduction in magnitude of velocity. When the circulation energy is unable to maintain the size and shape of vortex ring, the vortex ring breaks and there is a rapid fall in the magnitude of velocity. The centerline velocity profile for AR2 orifice at $f = 1$ Hz shows an undulation in the mid region in Fig. 13(a). A sudden fall in velocity magnitude occurs after $X/W = 1.5$ due to the transverse growth of vortex ring (see Fig. 5). A hump is formed before the splitting of vortex ring at $X/W = 5$. After $X/W = 6$, the bifurcated vortex rings move away from the centerline and a steep negative slope is observed. The overall pattern of velocity variation at 2 and 6 Hz (see Figs. 14(a) and 15(a)) is almost similar to those at $f = 1$ Hz (Fig. 13(a)). Since, the diaphragm displacement remains constant at a fixed actuation frequency, same amount of fluid is ejected out from the cavity in same time-period irrespective of the orifice geometry. Even though the cross-sectional area of AR2 is larger than that of AR1, the centerline velocity is higher for AR2 at 2 Hz and 6 Hz of actuation between $X/W = 1$–9. One possible reason behind this could be the change in aspect ratio of the orifice affecting the velocity distribution at the orifice exit (see variation of $U_f$ and $U_r$ at different frequencies in Fig. 9). Near the orifice exit, the shorter side vortices of vortex ring moves faster than the central region of vortex ring. This situation favors the suction of ambient fluid close to the shorter side of orifice as compared to the central region of orifice. It also reduces the effect of suction stroke close to the core or central region of vortex ring during its evolution. Another plausible cause behind this could be the length scale of the axial switching (aspect ratio) which controls the amplitude and distribution of velocity fluctuation. The formation of a trailing jet or closely spaced vortex rings may increase or decrease the time-averaged mean velocity. Therefore, even though the AR1 orifice has a higher convection velocity than AR2 orifice, for same actuation frequency (fluid expulsion in same time-period) the time mean velocity for AR2 orifice can be more or less in comparison to AR1 orifice depending on actuation frequency. The partial vortex formation and early breakdown of vortex ring due to differential self-induced, ejected fluid accumulate close to the orifice at 1 Hz and a cluster of tiny vortex rings are formed at $f = 2$ Hz for AR4 orifice (see Fig. 8). Therefore, velocity increases till $X/W = 2$ followed by a sudden drop at $f = 1$ Hz (see Fig. 13(a)) and an gradual increases in velocity till $X/W = 8$ at $f = 2$ Hz (Fig. 14(a)) is observed for AR4 orifice case.

The non-dimensionalized velocity distribution (see Figs. 13(b)–15(b)) for AR1 orifice at all frequencies in the transverse direction at different spanwise locations are identical, indicating the existing self-similarities of the velocity variation beyond $X/W = 1$. However, at the same actuation frequency (constant volume of fluid ejection) of 1, 2 and 6 Hz, AR2 and AR4 orifices show a wide fluctuations in velocity and the velocity field is far from reaching any self-similar pattern as evident from Figs. 13(c, d)–15(c, d). The synthetic jet spreads more in vertical (Z) direction as compared to the horizontal transverse (Y) direction for AR2 orifice in Fig. 13(c) and the nature of velocity distribution confirms the bifurcation process observed in Fig. 5. A sudden drop in velocity profile is seen at the location where vortex splitting is observed. At $f = 2$ Hz in Fig. 14(c) for AR2 orifice, the higher

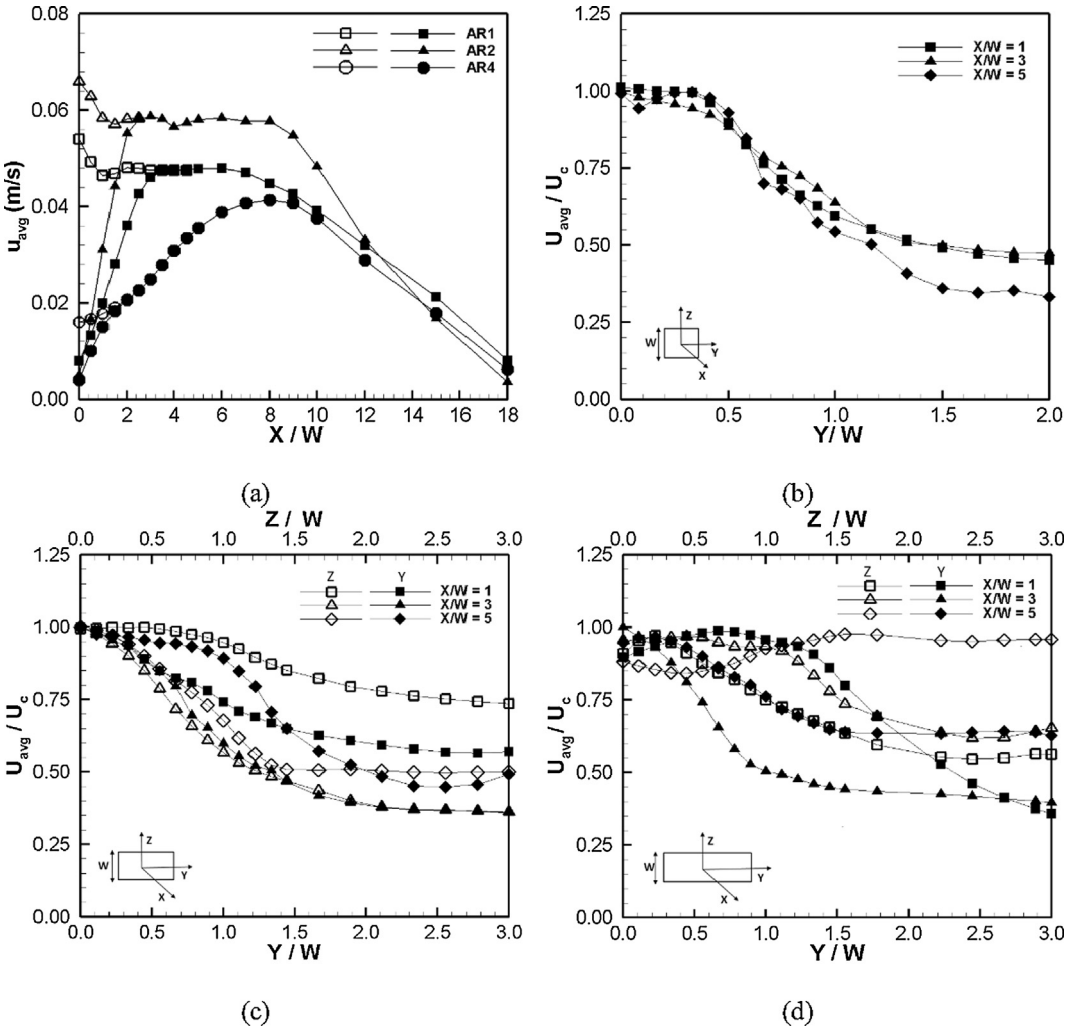


**Fig. 14.** (a) Time averaged mean stream wise velocity profile in X-direction at $f = 2$ Hz without correction of suction velocity (solid symbols) and with correction (hollow symbols) for different aspect ratio orifices. Normalized velocity profile at $f = 2$ Hz for (b) AR1 orifice in Y-direction, (c) AR2 and (d) AR4 orifice in Y and Z-direction at different downstream locations ($X/W$). Filled symbols represent Y-variations and hollow symbols represent Z-variations of velocity in (c) and (d).

value of velocity until $Z/W = 1.0$ at $X/W = 1$ location with a decay of velocity at $X/W = 3$ and 5 location indicates the trend of bifurcation in the vertical direction, followed by immediate breakup. This breakup causes more spreading and thus a higher value of velocity in Y-direction at $X/W = 5$ in comparison to $X/W = 1$ and 3. In Fig. 15(c), the velocity distribution is flattened more in transverse direction that illustrates a high rate of dissipation at 6 Hz of actuation.

Fig. 13(d) illustrates the case of AR4 orifice at 1 Hz actuation and it shows that the lower value of formation number ($L/D_h = 1.16$) limits the circulation of vortex ring. In addition, the longer side of vortex ring moves slowly near the orifice center as compared to the shorter side which results in a low and flattened velocity after $Z/W = 0.5$ in the vertical and a peak at $Y/W = 1$ in the transverse direction at a streamwise location of $X/W = 1$. This is also corroborated by the LIF images for AR4 at $f = 1$ Hz, where the vortices formed at the center are ingested back in the suction stroke and the vortices at shorter side (near $Y/W = 1$) move towards the center of the synthetic jet. This moving vortices towards the center spreads in the XZ–plane which leads to higher velocity for longer period at $X/W = 3$ in the vertical Z-direction. The velocity distribution at $f = 2$ and 6 Hz in Figs. 14(d) and 15(d) approximately follows the similar velocity distribution at $X/W = 1$, 3 and 5 in both directions.

A generic and inclusive conclusion can be drawn from the observations presented above. The change in the aspect ratio plays a crucial role in the velocity variation of different segments of the evolving vortex ring, thereby impacting the formation, stability, propagation and spreading of vortex rings. A larger aspect ratio of orifice produces greater velocity variations between vortices at longer and shorter side of the orifice, which leads to either bifurcation (AR2 orifice cases) or break-up of vortex ring into small vortex segments in the neighborhood of orifice. For the considered case, a greater spreading of synthetic jet is observed in the plane parallel to the shorter side of the rectangular orifice. The entrainment of the synthetic jet with surrounding fluids is likely to increase with aspect ratio but the penetration in downstream direction decreases. In the frequency range tested, the effect of actuation frequency on the flow field of synthetic jet is more pronounced for AR2 orifice as compared to AR1 or AR4 orifices.

### 3.4. Power spectral density

Next, Fast Fourier Transformation (FFT) spectra is computed for studying the characteristic energy content of the vortex structures present in the flow. Fig. 16 below presents the FFT spectra of stream wise velocity at various axial locations along the synthetic jet centerline for the four cases of vortex evolution considered before. Naturally, it is expected that the magnitude of the first harmonic value (actuation frequency) must be greater than the magnitude of the second harmonic. However, the presence of the suction velocity in the flow field leads to

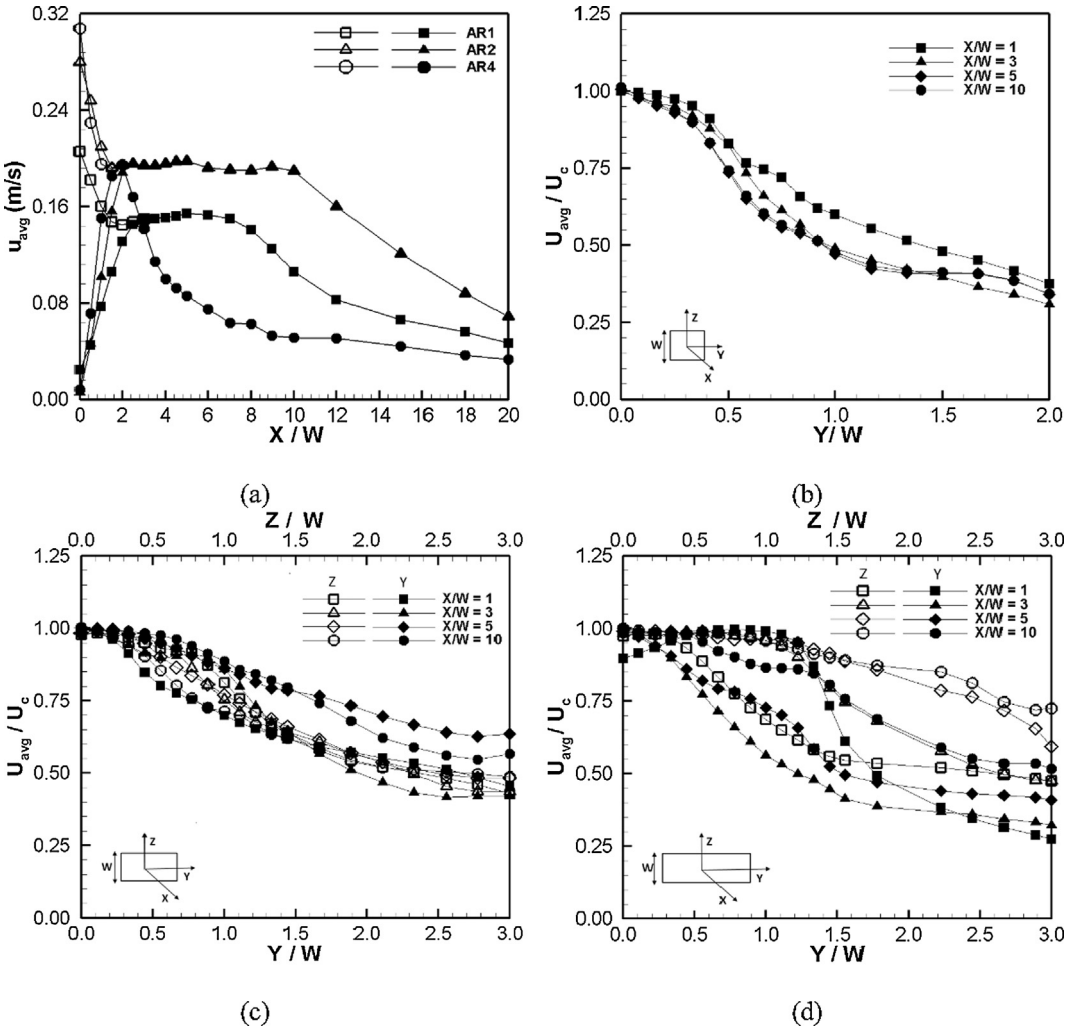


**Fig. 15.** (a) Time averaged mean stream wise velocity profile in X-direction at $f$ = 6 Hz without correction of suction velocity (solid symbols) and with correction (hollow symbols) for different aspect ratio orifices. Normalized velocity profile at $f$ = 6 Hz for (b) AR1 orifice in Y-direction, (c) AR2 and (d) AR4 orifice in Y and Z-direction at different downstream locations ($X/W$). Filled symbols represent Y-variations and hollow symbols represent Z-variations of velocity in (c) and (d).

additional peaks in the velocity signal or time trace (see Fig. 12), and this causes the apparent additional frequency in the spectra along with the second harmonic, thereby amplifying the amplitude of the second harmonic even beyond that of the first harmonic. This effect however, diminishes in the downstream direction as the effect of the suction dwindles in the streamwise direction. When $f$ increased from 1 Hz to 4 Hz for AR1 orifice in Fig. 16(b), the difference in the magnitude of first and second harmonic decreases. Similar trend is also observed for AR2 and AR4 orifices when frequency is increased from 1 Hz to 6 Hz respectively. A large variation between the magnitude of first harmonic and second harmonic is present at the orifice exit for AR2 actuating at 1 Hz similar to AR1 and AR4 orifice case at same actuation frequency, due to the directional insensitivity of hot-film. When a vortex ring escapes out from the suction zone, the centerline velocity increases (see Figs. 13(a)–15(a)) and subsequently an increase in the magnitude of the first harmonic is observed as well. As it can be seen from the figure, for the AR1 orifice at $f$ = 4 Hz, the difference between the magnitude of first and second harmonic is less as compared to the other three cases for orifice AR1 and AR2 actuated at $f$ = 1 Hz. The presence of coherent structures at different length scales can be identified by presence of discrete peaks at multiples of harmonic frequencies. These peaks at multiples of actuation frequency in FFT plot at different locations in downstream direction confirm the pulsating behavior of the synthetic jet.

Further, the distribution of energy associated with velocity signal measured along the jet centerline provides information about the vortex ring propagation, breaking and dissipation. The magnitude of spectral density at first harmonic ($f$) and second harmonic ($2f$) in downstream direction along the synthetic jet centerline is shown in Fig. 17 for AR1 and AR2 orifice at all the actuation frequencies. The difference between the first and second harmonic spectral density indicates the suction effect in the near field region. The magnitude of the first harmonic and second harmonic are weak due to breaking of vortex ring near the jet exit region for AR = 4. The power spectral density for AR2 orifice shows higher value of second harmonic spectral density compared to that of first harmonic near the orifice exit region for $f$ = 1 Hz, which indicates a strong effect of suction stroke at center of orifice as compared to the AR1 orifice. The nature of spectral magnitude distribution for first harmonic is nearly same for both AR1 and AR2 orifice case at $f$ = 2 Hz in Fig. 17(b). The harmonic values decreases in downstream direction and beyond $X/W$ = 6, the spectrum is similar to a fully developed boundary layer spectrum. The difference between the first and second harmonic spectral value reduces as the frequency is increased from 2 Hz to 6 Hz (see Fig. 17(b)–(d)). In the axial switching of vortex ring, the fluctuation in centerline velocity depends on the ratio of major to minor axis of vortex ring. The undulation of average centerline velocity for AR2 orifice is more clear and distinct than that of AR1 orifice case (see Figs. 13(a)–15(a)) and subsequently a large undulation is

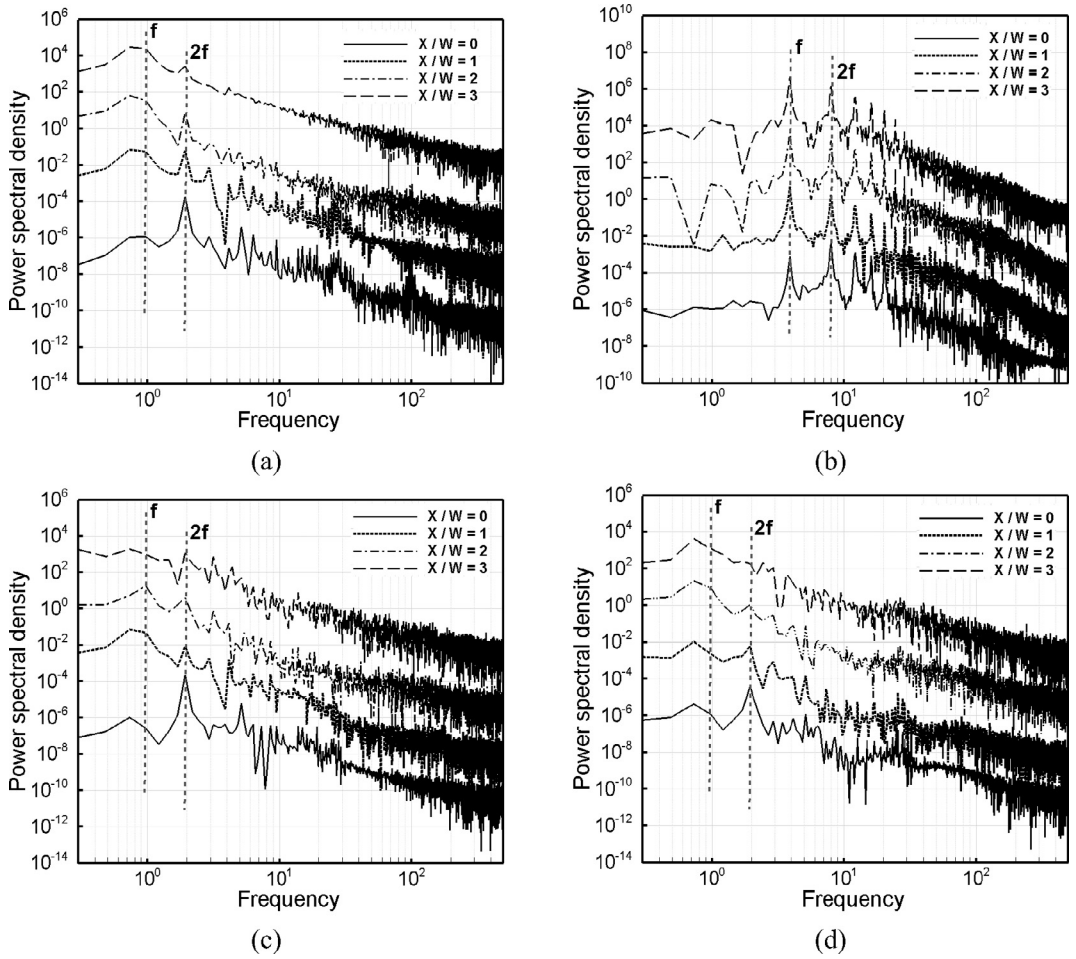


**Fig. 16.** Power spectral density distribution of stream wise velocity component at different span wise locations ($X/W$ = 0, 1, 2, 3) in downstream direction for: (a) AR1 orifice at 1 Hz, (b) AR1 orifice at 4 Hz, (c) AR2 orifice at 1 Hz and (d) AR4 orifice at $f$ = 1 Hz along jet exit centerline. The power spectral density curves at $X/W$ = 1, 2, and 3 are shifted upwards in multiple of $10^3$ from the curve at $X/W$ = 0.

observed in the spectral density distribution of Fig. 17. The convection velocity of vortex ring increases and the vortex ring switches its axis more rapidly, which can be easily distinguished from the number of undulation in peak power spectral density (Fig. 17) compared to average centerline velocity profile. For all the cases shown in Fig. 17, the power spectral density is negligible after $X/W$ = 12, suggesting that the synthetic jet loses its coherency at this streamwise location.

## 4. Conclusions

The present study reports the flow characteristics of synthetic jet as a function of aspect ratio of the rectangular orifice focusing particularly on the phenomenon of vortex bifurcation and the underlying flow physics. LIF imaging is used to visualize the flow structure of the synthetic jet. Hot-film is used for measuring the velocity field of the synthetic jet for quantitative analysis. Initially, experiments are carried out with the circular orifices and it was found out that the flow physics captured with our measurements match closely with that of studies reported in the literature (such as [16]). Next, experiments are carried out with the rectangular orifices, keeping the hydraulic diameter constant while the aspect ratio is varied as 1, 2, and 4. The experiments are carried at discrete values of actuation frequency 1, 2, 4, and 6 Hz with oscillation amplitudes of 0.23, 0.34, 1.34 and 1.72 mm respectively. The important observations from the present study can be summarized as follows:

- For the same amount of volumetric ejection through different orifice geometries, the flow structures change substantially, depending upon the actuation frequency and aspect ratio of the orifice. $L/D_h$ ratio is the most important parameter that characterizes the flow physics of the synthetic jet. Upon visual observations, the obtained flow structures can be broadly grouped into four distinct regimes, irrespective of orifice shape, such as: partially ejected vortex ring, vortex ring without a trailing jet, vortex ring with a strong trailing jet and vortex ring bifurcation. The study shows that a vortex overshoot is present close to the orifice, followed by axial switching or bifurcation depending on position of counter rotating vortices in orthogonal planes.
- The phenomenon of vortex splitting and bifurcation was observed only for a rectangular orifice of aspect ratio 2 (AR2) in a particular $Re$ range (for example, corresponding to 1 Hz). The reason behind the vortex bifurcation was explored and through experimental measurements, it was established that the vortex splits into two halves due to two reasons: First, a large disparity between the velocities of vortex core and the center of the vortex ring, $U_r$ and $U_f$, respectively and second, the time lag in which the separation distance between the counter-rotating vortices decrease gradually to zero. The distribution of stream wise velocity component at the orifice exit coupled with the suction effect of the following cycle predicts the bifurcation of vortex ring in synthetic jet. The positive velocity gradient for a longer distance in one transverse plane with a steep negative velocity gradient in another transverse plane at different locations in downstream direction confirms the bifurcation of synthetic jet.

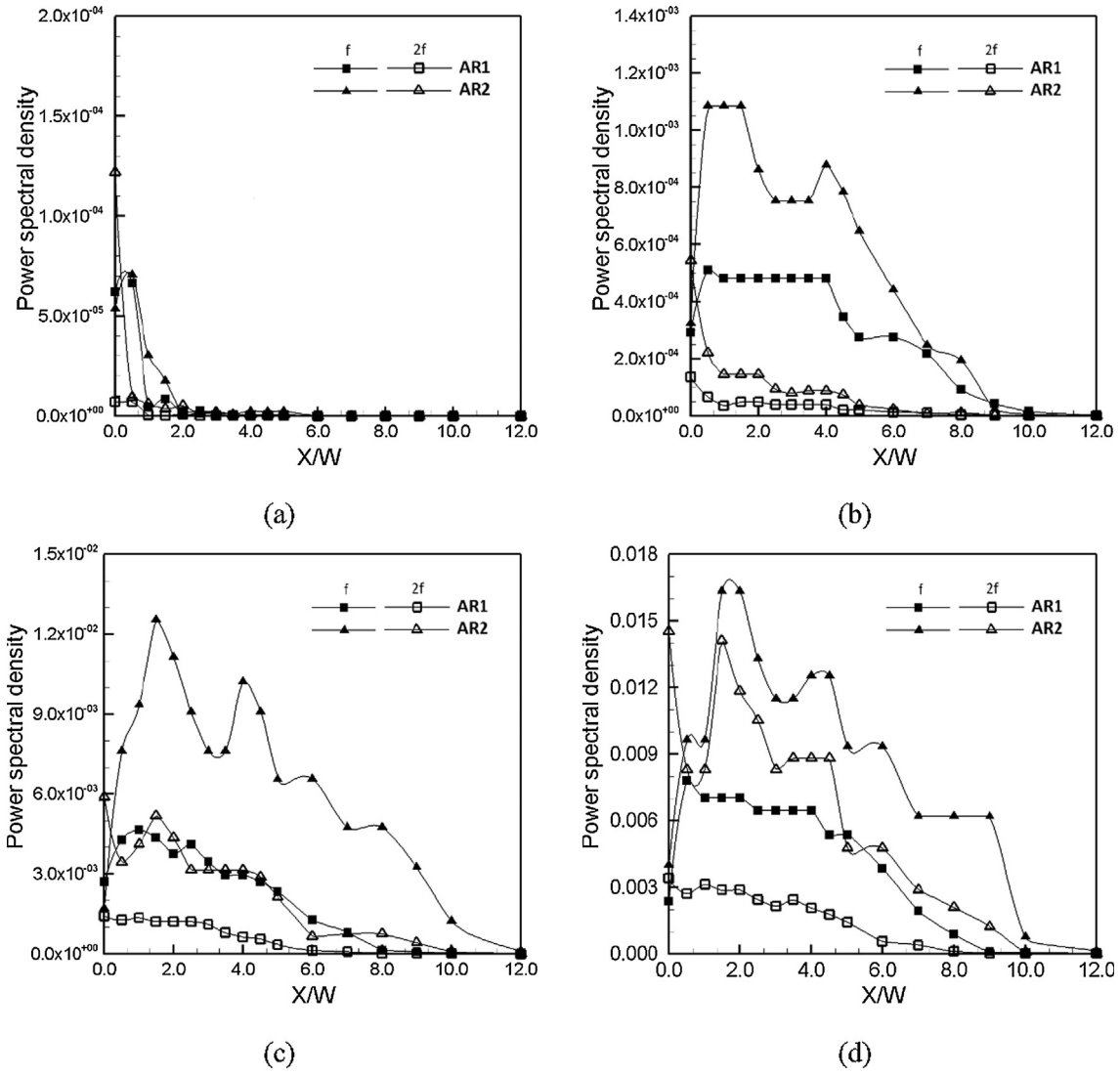


**Fig. 17.** The peak power spectral density variation in downstream direction ($X/W$) along jet centerline at actuation frequency (solid symbols) and second harmonic (hollow symbols) for AR1 and AR2 orifices at actuation frequencies: (a) 1 Hz, (b) 2 Hz, (c) 4 Hz and (d) 6 Hz.

- Velocity time trace is studied to explore which of the orifice shapes (or aspect ratios) are more susceptible to bifurcation. Both orifice size, shape and frequency of actuation affect velocity time trace in the orifice downstream.
- The computation of time-averaged velocity suggests that the change in the aspect ratio plays a vital role in the velocity variation of the different segments of the vortex rings, thereby impacting the formation, stability, propagation and spreading of vortex rings. A larger aspect ratio of orifice produces larger velocity variations between vortices generated from longer and shorter side of the orifice, leading to either bifurcation or breakup of vortex ring into small vortex segments in the neighborhood of orifice. In general, it was noticed that a greater spreading of synthetic jet is observed in the plane parallel to the shorter side of the rectangular orifice. The entrainment of the synthetic jet with surrounding fluids increases with aspect ratio, but the penetration in the downstream direction decreases. Finally, the effect of the actuation frequency on the flow field of the synthetic jet is more pronounced for AR2 orifice, as compared to AR1 or AR4 orifice.
- Power spectral density of the velocity signals indicates that the suction effect of the preceding cycle is present only till $X/W = 3$, although the coherent structures can be found to exist to a much farther distance of $X/W = 10$. Beyond this distance, the flow structures are dissipated and the power spectral density is negligible. This limits the working range between $X/W = 3$–10 in the downstream of a synthetic jet.

Finally, the current study was motivated by exploring the experimental conditions and the physics behind the intriguing phenomenon of vortex bifurcation and to characterize the rectangular orifice synthetic jet. The present study thus, provides some insights into the flow physics of the synthetic jet across a range of experimental parameters and some possible reasons behind vortex splitting has also been suggested. However, to fully understand the mechanism of the vortex bifurcation and substantiate it based on the physical measurements requires more detailed experiments to be carried out, and can be taken up in future studies.

## Conflict of interest

The authors declare no conflict of interest in the publication of this manuscript.

## Acknowledgment

Naval Research Board (NRB), DRDO, Government of India

supported this research and their support is gratefully acknowledged. The authors also acknowledge the facility of water tunnel research laboratory, Indian Institute of Technology Kanpur for facilitating in carrying out the experiments.

## References

[1] M. Amitay, D.A. Pitt, Separation control in duct flows, J. Aircr. 39 (2002) 616–620, https://doi.org/10.2514/2.2973.
[2] M. Amitay, A. Honohan, M. Trautman, A. Glezer, Modification of the aerodynamics characteristics of bluff bodies using fluidic actuators, 28th AIAA Fluid Dyn. Conf. Snowmass, Colorado 97-2004, 1997. < https://doi.org/10.2514/6.1997-2004 > .
[3] M. Amitay, D. Smith, V. Kibens, D. Parekh, A. Glezer, Modification of the aerodynamics characteristics of an unconventional airfoil using synthetic jet actuators, AIAA 39 (2001) 361–370, https://doi.org/10.2514/2.1323.
[4] P. Anna, M. Amitay, Electronic cooling using synthetic jet impingement, J. Heat Transf. 128 (2006) 897–907, https://doi.org/10.1115/1.2241889.
[5] D. Auerbach, T. Grimm, Factors influencing the non-circular ring vortex motion, Meccanica 29 (1994) 351–359, https://doi.org/10.1007/BF00987570.
[6] M. Chaudhari, B. Puranik, A. Agrawal, Effect of orifice shape in synthetic jet based impingement cooling, Exp. Therm Fluid Sci. 34 (2010) 246–256, https://doi.org/10.1016/j.expthermflusci.2009.11.001.
[7] A. Crook, N. Wood, Measurements and visualisation of synthetic jets, 39th Aerospace Sciences Meeting and Exhibit, 2001. < https://doi.org/10.2514/6.2001-145 > .
[8] J.B. Freund, P. Moin, Jet mixing enhancement by high-amplitude fluidic actuation, AIAA J. 38 (2000) 1863–1870, https://doi.org/10.2514/2.839.
[9] P. Fung, M. Amitay, Active flow control application on a mini ducted fan UAV, J. Aircr. 39 (2002) 561–571, https://doi.org/10.2514/6.2001-2440.
[10] M. Gharib, E. Rambod, K. Sariff, A universal time scale for vortex ring formation, J. Fluid Mech. 360 (1998) 121–140, https://doi.org/10.1017/S0022112097008410.
[11] A. Glezer, M. Amitay, A. Honohan, Aspects of low and high-frequency actuation for aerodynamic flow control, AIAA 43 (2005) 1501–1511, https://doi.org/10.2514/1.7411.
[12] T.B. Gohil, A.K. Saha, K. Muralidhar, Control of flow in forced jets: a comparision of round and square cross sections, J. Visual. 13 (2010) 141–149, https://doi.org/10.1007/s12650-009-0020-7.
[13] F.F. Grinstein, Entrainment and transition to turbulence in subsonic rectangular jets, Reno, NV, 33rd Aerospace Sciences, 1995. < https://doi.org/10.2514/6.1995-861 > .
[14] F. Hussain, H.S. Hussain, Elliptic Jets, Part 1. Characteristics of unexcited and excited jets, J. Fluid Mech. 208 (1989) 257–320, https://doi.org/10.1017/S0022112089002843.
[15] S. Iio, T. Kawamura, M. Matsubra, T. Yoshida, T. Ikeda, Vortex behavior of a pulsating jet from rectangular nozzle, JSME Int. J. 49 (2006) 989–994, https://doi.org/10.1299/jsmeb.49.988.
[16] M. Jabbal, J. Wu, S. Zhong, The performance of round synthetic jets in quiescent flow, Aeronaut. J. 110 (1108) (2006) 385–393, https://doi.org/10.1017/S0001924000001305.
[17] P. Jagadeesh, K. Murli, V. Idichandy, Experimental investigation of hydrodynamic force coefficients over AUV hull, Ocean Eng. 36 (2009) 113–118, https://doi.org/10.1016/j.oceaneng.2008.11.008.
[18] J.J. Ai, S.C.M. Yu, A.W.K. Law, L.P. Chua, Vortex dynamics in starting square water jets, Phys. Fluids 17 (2005) 1–12, https://doi.org/10.1063/1.1823532.
[19] K. Mohseni, Pulsatile vortex generators for low-speed, Ocean Eng. 33 (2006) 2209–2223, https://doi.org/10.1016/j.oceaneng.2005.10.022.
[20] B.L. Smith, A. Glezer, Jet vectoring using synthetic jets, J. Fluid Mech. 458 (2002) 1–34, https://doi.org/10.1017/S0022112001007406.
[21] Y. Utturkar, R. Holman, R.l. Mitta, B. Carroll, M. Sheplak, L. Cattafesta, A jet formation criterion for synthetic jet, AIAA 41st Aerospace Sciences Meeting & Exhibit, 2003. < https://doi.org/10.2514/6.2003-636 > .
[22] M. Watson, A.J. Jaworski, N.J. Wood, A study of synthetic jets from rectangular and dual circular orifices, Aeronaut. J. (2003) 427–434, https://doi.org/10.1017/S000192400001335X.
[23] K. Zaman, Axis switching and spreading of an asymmetric jet: the role of coherent structure dynamics, J. Fluid Mech. 316 (1996) 1–27, https://doi.org/10.1017/S0022112096000420.